1-1-2012

H-Alpha Narrow Band Filter Commissioning And Imaging At The UND Observatory

Rakesh R. Nath

H-ALPHA NARROW BAND FILTER COMMISSIONING AND IMAGING AT THE UND OBSERVATORY

By

Rakesh Nath

Bachelor of Engineering, Vishweshraya Technological University (VTU),2007

A Thesis

Submitted to the Graduate Faculty

Of the

University of North Dakota

In partial fulfillment of the requirements

For the degree of

Master of Science

Grand Forks, North Dakota

August

2012

This thesis, submitted by Rakesh Nath in partial fulfillment of the requirements for the Degree of Master of Science from the University of North Dakota, has been read by the Faculty Advisory Committee under whom the work has been done, and is hereby approved.

Name of Chairperson

DR. PAUL S. HARDERSEN

Name of Committee Member

DR. VISHNU REDDY

Name of Committee Member

DR. K.S. BALASUBRAMANIAN

This thesis is being submitted by the appointed advisory committee as having met all of the requirements of the Graduate School at the University of North Dakota and is hereby approved.

WAYNE SWISHER
Dean of the Graduate School
07/11/2012
Enter the Date

Title H-alpha Narrow Band Filter Commissioning and Imaging at the UND Observatory

Department Space Studies

Degree Master of Science

In presenting this thesis in partial fulfillment of the requirements for a graduate degree from the University of North Dakota, I agree that the library of this University shall make it freely available for inspection. I further agree that permission for extensive copying for scholarly purposes may be granted by the professor who supervised my thesis work or, in his absence, by the Chairperson of the department or the dean of the Graduate School. It is understood that any copying or publication or other use of this thesis or part thereof for financial gain shall not be allowed without my written permission. It is also understood that due recognition shall be given to me and to the University of North Dakota in any scholarly use which may be made of any material in my thesis

Rakesh Nath
07/11/2012

TABLE OF CONTENTS

LIST OF FIGURES

LIST OF TABLES

ACKNOWLEDGMENTS

I wish to express my sincere appreciation to the members of my advisory committee and faculty for their guidance and support during my time in the Masters program of Space Studies at the University of North Dakota.

To my Dad, family, friends and the larger scientific community who have been the pillar of support for this thesis.

ABSTRACT

The University of North Dakota (UND) Observatory will commence solar observations with the commissioning of a DayStar 0.4-Angstrom Hα filter attached to a Meade LX200 Schmidt-Cassegrain telescope. Imaging will occur using a Finger Lakes Instrumentation PL16803 front illuminated, monochrome CCD/filter wheel with a neutral density filter. An interference eliminator is also present in the optical train. This effort is part of a larger effort to develop an independent, externally-funded solar physics group at UND. This work is the first effort at gaining direct experience with solar instrumentation, observations, calibrations, and post-image processing. The primary goals of this Master's thesis project at the UND Department of Space Studies is to a) qualitatively evaluate site seeing and b) apply a variety of image processing algorithms to attempt to better define the dimensions of chromospheric features. A critical aspect of this effort will be to evaluate the scientific usefulness of the resulting datasets. This program will lay the foundation for an ISOON-like system at the UND Observatory that will provide continuous and automated solar monitoring. Images will be acquired, calibrated on-the-fly, and posted to the UND Observatory web site. An image archive will be created and an image portal developed that will provide public access to the acquired images.

Chapter I: Introduction

This thesis is the first attempt of the University of North Dakota (UND) Observatory to commission and operate an instrument to conduct observations of the Sun. This thesis involves the commissioning and imaging of the Sun using a Daystar Hα filter. The Daystar Hα filter is the first in its kind of narrow band filters employed by UND to do scientific imaging.

The primary goal of this thesis is to obtain as many images as possible, attempt flat fielding and calibration techniques to improve the image quality. The idea is to observe how the seeing varies over the day. A secondary goal is to apply various image processing techniques and see how image processing affects the image quality.

This thesis has conducted an imaging procedure over a period of three days at the UND Observatory for the imaging process. These images were subjected to flat division and dark subtraction. This thesis attempts to quantify the seeing by observing the change in resolution of a particular feature over a certain number of images.

This thesis has attempted a number of image processing techniques attempting to improve the contrast in the images. This will document the image processing techniques attempted and evaluate their usefulness.

Chapter II. Literature Review

Introduction

The Sun is the most obvious astronomical sight in the daytime. The Sun's surface displays a number of different kinds of features varying from magnetic sunspots to solar flares. It is important to understand the nature of these features in order to understand the physics of the Sun. As these features appear on the Sun as a result of internal processes, it is prudent to first understand how the Sun is structured. The general structure of the Sun in outlined in Figure 1:

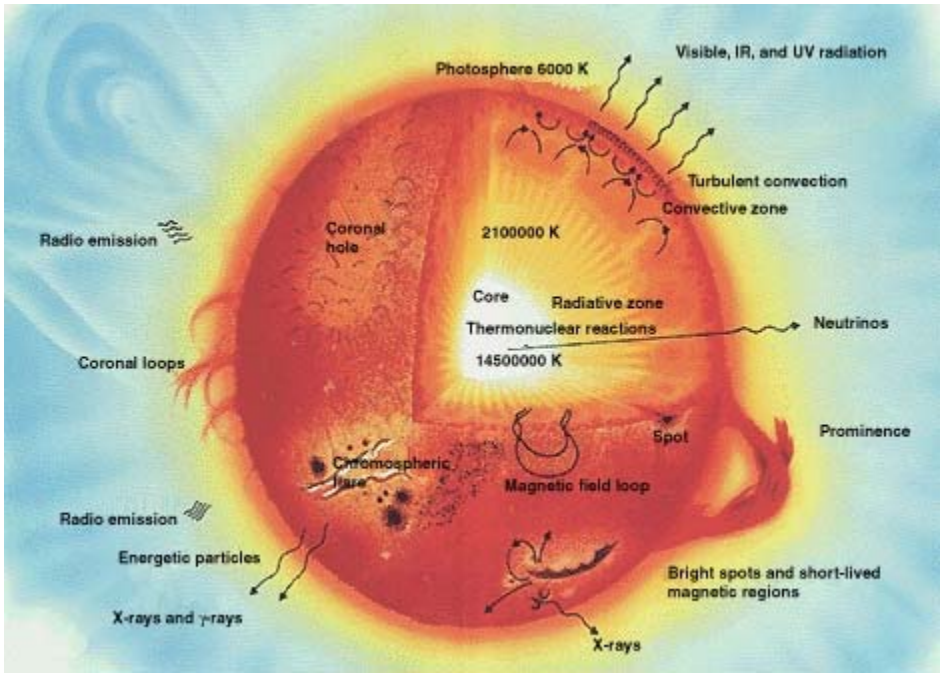

Figure 1: Structure of the Sun. The structure of the Sun is divided into a number of regions in this figure showing representative features in each region, the temperature

gradations are shown varying from the core to the surface of the Sun. Source: Hamilton(2004)

The Sun is a G-type spectral star that is divided into a number of layers which appear as regions demarcated theoretically. Though the regions of the Sun are clearly demarcated, as shown in Figure 1, the regions themselves are not stratified layers but appear as gradations in the overall structure of the Sun. The Sun is modeled into different regions based on the temperature of each layer of gas. These different regions of the Sun also radiate in specific wavelengths at specific depths to the solar core.

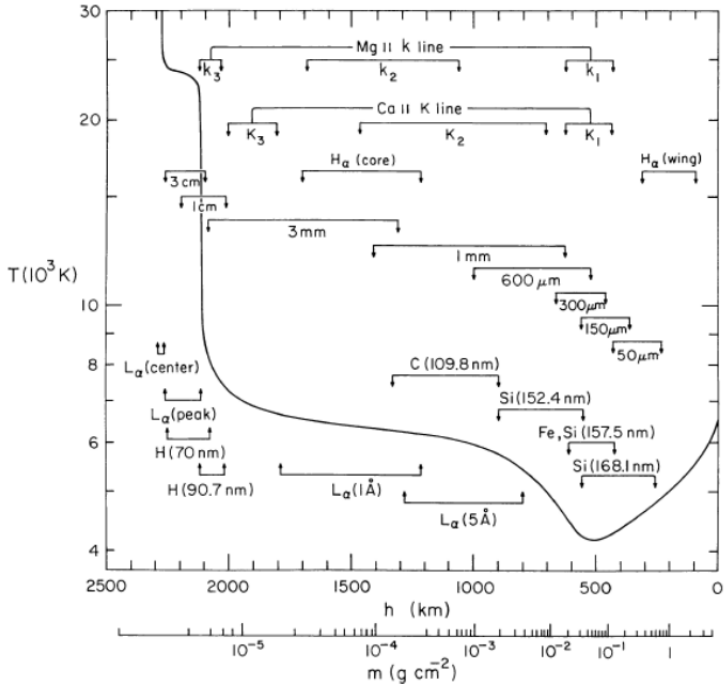

Figure 2: Temperature gradations from the solar surface. The density gradations are shown below the x-axis which indicates the change in density from the photosphere to the corona. Source: Vernazza (1973)

These zones may be characterized by their ranges of temperature and also by the mode of energy transport through them.

- The *core* is the hot, dense central region in which the nuclear reactions that power the Sun take place. It comprises about 20% of the interior radius (Ryan and Norton (2004)). The temperature of the core is roughly about 15,000,000 K.
- The *radiative zone is located* from about 20% to 70% (Ryan and Norton (2004)) of the solar radius. This zone is where the primary mechanism of energy transfer happens radiatively and the transfer of energy is determined by radiative transfer equations.
- The *convective zone* starts at about 70% (Ryan and Norton (2004)) of the solar radius and extends to just below the surface. The convective zone is the region where the high velocity, high energy photons from within the solar core encounter cooler gas and the gas molecules. Instead of getting excited and ionized, the gas molecules trap the energy and transfer it in the form of convection currents.
- At a distance of 1 solar radius of about 6.96×10^6km the mass of the overlying layers balances the gas pressure and the resulting thermodynamic equilibrium produces a surface. This is known as the photosphere and represents the visual disk that is visible in the continuum spectrum.
- Beyond this point are what is called the outer regions of the solar atmosphere comprising the chromosphere, transition region and the corona.
- The chromosphere is the thin layer of gas that envelopes the Sun as shown in Figure 1 where the chromospheric flares are indicated and Figure 2 indicates this layer as the extent of the Hα spectrum. Roughly this would extend to about 2000km above the photosphere.

- The transition region and corona are the regions in Figure 2 where the sharp spike in temperature is noted at about 2200 km above the photosphere.

The Sun is divided into a number of regions based on the distance from the center, the density of the layer and its temperature. The density indicates how much material resides in the particular layer and its distribution. As we move outwards from the core, the density decreases and the temperatures drop. The ionized plasma condenses to gas molecules, and the gas starts playing a role in physics of the solar features. One notices a dominance of gas laws and magnetic field theory over quantum mechanics going from the core to the surface of the sun. This change in the behavior of the physical systems is seen explicitly in the chromosphere and specifically in chromospheric features. The chromosphere is located in the upper atmosphere of the Sun, beyond the photosphere and below the corona and transition region.

What is the chromosphere?

At one time, the chromosphere was visible only during an eclipse. This was how the chromosphere got its name: it was the rose colored narrow ring surrounding the Sun during the eclipse (Mullan (2010)). The chromosphere therefore was visible only for the couple of seconds when the Sun was getting eclipsed. Since this layer was colored it was named the "color-sphere" or chromosphere. A flash spectrum—a spectrum that lasts only a few seconds-- of the chromosphere reveals a large number of emission lines in the spectrum. The emission lines noticed in such a flash spectrum were those of the Hα, Hβ, Hγ and Hδ with wavelengths of 6563, 4861, 4340 and 4102 Å respectively. These emission lines of Hydrogen merely indicate the presence of Hydrogen in the spectra; bound electrons in the gaseous atoms move from a higher energy level to a lower one, in

the process release their energy in the form of light at the corresponding de-Broglie wavelengths. This is the emission mechanism in the corresponding band lines; however it may happen that at the same wavelengths the energy is absorbed by the hydrogen electrons at the same orbital energy levels resulting in an absorption spectrum. The region where emissions and absorptions happen at the indicated wavelengths is the chromosphere. The chromosphere extends as shown in Figure 2 to a height of 2000km above the photosphere. Lockyer (1868) gave what is today considered the most comprehensive definition of the chromosphere:

> "The term Chromosphere is suggested for this envelope [of gases], in order to distinguish it from the cool absorbing atmosphere on the one hand, and from the white light-giving photosphere on the other."

The chromosphere stands out in the Hα most prominently because of the presence of a forest of spicules on the limb and the presence of prominences which emits in the Hα and its wings.

A historical perspective

Father Secchi in 1877 first estimated the length of protuberances from the chromosphere, which were then known as flames, today as spicules, to be about 100-300 km. The modern estimate is about 800 km (Bhatnagar (2008)). Pierre Jules Jannsen was the first to employ a spectrograph to observe these spicules. Jannsen's observations triggered the idea of looking for specific elements in the spectrum and a flash spectrum performed in1868 revealed the presence of helium in the chromosphere. The next couple of decades saw a burst of activity in the observation of emission lines in the solar spectrum. Evershed detected 313 different emission lines Bhatnagar (2008), including the

entire Balmer series. Observations of the chromosphere in the Hα by Nikolsky (1970) showed that the width of spicules were close to 1000km and that they can extend upto a height of about 20,000 km. Nikolsky and Platova(1971) estimated the spicules to have a velocity of 10-15 km/s. The modern estimates of these data are roughly the same; although their widths have been refined to be between 200 and 1000km by De Pontieu et al(2007).

Another Hα feature is a prominence, seen "prominently" on the limb of the Sun. Prominences were first observed as structures standing above the limb of the Sun in the chromosphere. Prominences can be viewed on the solar disk in the Hα spectrum and are called filaments. They appear as dark ribbon-like structures located preferentially where magnetic fields change their polarities. They can last for hours, days or weeks and sometimes towards the end of their lifetimes erupt into explosive events. They can erupt very rapidly and cause heating and expulsion of material into the upper atmosphere. Their causes are not yet fully understood but they have been observationally distinguished from spicules by their shapes and duration of existence. The prominences primarily radiate/absorb in the Hα spectrum. Prominences are further classified into quiescent and active prominences. Quiescent prominences are by far the most stable features on the Sun outside of the sunspots. (N. Labrosse(2010)). Quiescent prominences have been known to last from a few days to several months. Quiescent prominences have lengths of 10^4-10^5 km, 10^3-10^4 km in thickness and heights of 10^4-10^5 km. Figure 3 shows an example of a quiescent prominence with the size of the Earth as a reference.

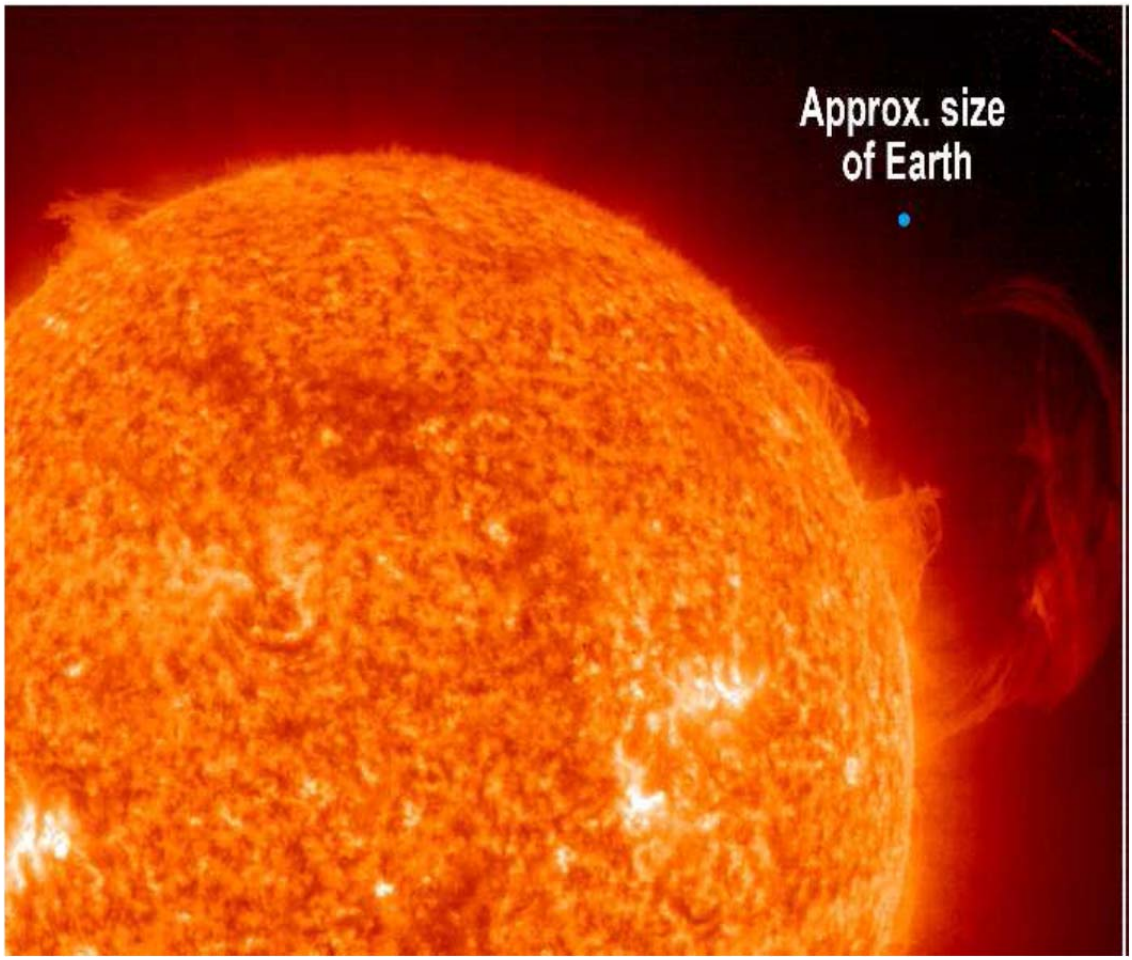

Figure 3: Quiescent prominence: The large prominence shown in the figure is an example of the quiescent prominence. The size of the earth is shown right next to this prominence to indicate the scale of the size of the prominence (N. Labrosse(2010)). Active prominences, on the other hand, are typically dynamic features occurring in the vicinity of active regions and are usually short-lived, usually lesser than the corresponding active regions.

Active Regions and Sunspots:

The evolution of sunspots in the chromosphere is directly related to the observation of features called Ellerman Bombs. Ellerman(1917) observed some features extending from 4- 10 Å on both sides of the Hα emission spectrum, but not crossing into the central emission line. These were described as "bombs" in the Sun. The "bombs" were initially thought to be the cause of solar flares and were initially observed to see

whether they could give a clue to predicting the flares. By the 1960's, however, this idea had died down. It is suspected that these bombs might influence the development and evolution of sunspots in the photosphere. Later Severny (1956) observed the same features as Ellerman(1917) and called them “mustaches”. Lyot(1944) photographed these features for the first time directly and found a large number of small, bright, circular areas in the close vicinity of sunspots. It was noted in many subsequent observations that these spots observed by Lyot, which he called “Petits points” have almost incontrovertibly been proven to be the same features that Ellerman had identified as bombs. These features are small and have historically been difficult to observe. The observed width of the bombs is about 0.4 arcseconds Lites(1986). These bombs tend to occur at the outer edges of the penumbrae of the larger sunspots. The next most common location these bombs are found is in the inter-spot area between sunspots. On an average the bombs last for about 10 minutes. The smallest duration bomb noticed by Lyot(1944) lasted about 4 minutes.

While these bombs were noticed on the edges of the sunspots, it is important to understand how the sunspots themselves were observed in the chromosphere. As the sunspots are photospheric phenomena, their effects on the chromosphere will give a clue to the vertical extents of the sunspots themselves and the active regions in general. Their influences are critical to the understanding of how the chromosphere connects with the photosphere and vice-versa. Lites(1986) reports that there are weak chromospheric oscillations during a cycle of umbral oscillations. The presence of oscillations at this point, Lites(1986) claims, can be used as an independent diagnostic of chromospheric

structure and energetics in sunspots. The oscillation frequency is driven by a specific photospheric resonance mechanism.

Initial chromospheric studies were limited to studying the umbrae as a spatially averaged profile of some Fraunhofer lines. Beckers et al(1960) claimed that they could see structures in the Ca_{II} H and K lines. These structures were short-lived and hence were called 'umbral flashes'. Beckers et al(1960) have also observed that the umbra has an effect several thousand kilometers high, that is, reaching into the chromosphere. The general opinion of Beckers et al(1960) is that umbral flashes are related to the tunneling of magneto-acoustic waves through the resonant cavity between the umbra and the chromosphere. It was generally observed that the umbral flashes themselves arise at the instants of maximum acceleration of the upward-directed material. One of the first assumptions made is that these oscillatory motions were purely vertical. However, Turova et al (1983) , suggest that there may be a tangential component to this velocity as well. A typical umbral flash is shown in Figure 4:

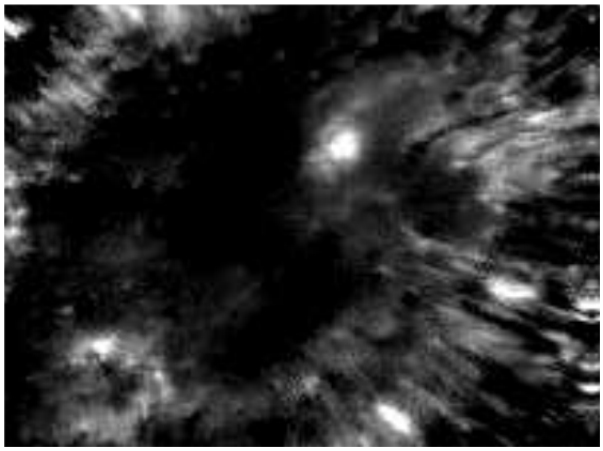

Figure 4: Umbral flash. An umbral flash is shown forming a ring like structure on the right extreme. Source: Socas-Navarro et al. (2001)

Some authors believe that the source of these acoustic oscillations lies immediately beneath the photosphere. However Socas-Navarro et al. (2001) suggest that the source lies much higher, at the photospheric level.

Flares and eruptions

Active regions and sunspots will eventually lead us to understand some of the violent expulsions of material from the Sun known as flares. Solar flares tend to be the result of the evolution of an active region. This active region could be either in the photosphere as a sunspot or a sunspot accompanied by a bright active region in the chromosphere. The question is what happens to the active region that erupts and how does the erupting material interact with the chromosphere, whose study this thesis is focusing on?

Solar flares increase the brightness of the chromospheric region they erupt out of, in the Hα spectrum. The primary reason for this is that during a solar flare the chromosphere is heated above its pre-flare value by different mechanisms. One of the mechanisms is that when energetic electrons are emitted during a flare, they are stopped by the chromosphere Milligan et al(2004). Coronal temperature measurements suggest that thermal conduction could be another reason for the heating Milligan et al(2004). The general hypothesis is that in the initial impulsive phase of the solar flare, accelerated electrons propagate along the closed loop magnetic fields to the dense underlying chromosphere. They lose energy via coulomb collisions and heat up the local plasma. The resulting expansion of the plasma is called chromospheric evaporation.

Plages

Plages are another set of features that seem connected to the evolution of sunspots and active regions, but their direct relation is not well known. Plages were noted as early as 1878 in spectroheliograms taken in the CaII, H and K lines which show large bright regions on the chromosphere. They appear in spectrograms of the Sun in the strong Fraunhofer lines and were compared to the quiet chromosphere.

Plages are described as a bright region on the Sun often associated with a sunspot and active regions generally as reported by Shine et al(1972). They don't seem to be isolated incidents but seem to be associated with sunspot activity on the photosphere. Plage radiation is the main source of solar Extreme Ultraviolet (EUV) that interacts with the Earth's upper atmosphere (Foukal(1988)).

Plages are visually simple to spot on the disk of the Sun. The excessive broadband radiation from these plages are brighter than the quiet chromosphere and outweigh the radiative deficit of dark sunspots thus explaining why solar irradiance increases near maxima of solar activity Foukal(1988)

Chromospheric Dynamics: Spicules

Two of the earliest papers on the spicules is by Athay,R.G.,(1958) and Zirker,J.B.,(1962) who talk of resolving the spicules in the Hα and D_3 helium line(587.56nm) simultaneously. Later it was apparent that spicules radiated primarily in the Hα, which made them popular high resolution Hα targets. Spicules are important dynamic entities because not only are they the most abundant feature on the chromosphere, but most of the radiation in the chromosphere is thought to be because of spicules. Spicules are also thought to be important entities in energy transport to the corona both through oscillations and energy deposition methods.

The idea of observing in these frequencies at that time was to measure the Doppler velocity and temperature of the spicules. Athay,R.G.,(1958) states that one of the reasons why spicules are poorly understood is because of the meager data available at the time on this topic. Athay (1958) reported that the Doppler velocity of spicules is 32 to 35 km/s. The helium-D_3 line on the other hand gives a Doppler velocity of 16 Km/s. The mean kinetic temperature for the D_3 and Hα together is 58,000^{o}C Athay (1958). Zirker (1962) reports the temperature of the spicules to be of the order of 50,000 K and the turbulent velocity to be about 8 km/s. The major issue that Zirker (1962) finds is that the inter-spicular area is very difficult to define, due to the poor seeing, as the region is heavily populated with light from spicules and surrounding spicule-clusters. The modern view of Athay(2000) and DePontieu(2007) is that spicules can reach a height of 10,000 km with velocities varying between 10 and 30 km/s. DePontieu(2007) also states that there is a probability that the spicules serve as material transport entities between plages of opposing polarities. Also various high resolution spacecrafts have identified new features such as mottles, fibrils and loops DePontieu(2007). But it is unclear whether these are associated with spicules. Analysis of magnetogram data by Lopez-Ariste and Casini (2005) reveals that spicules can have magnetic field strengths of about 10G at heights of 3500km. However Trujillo-Bueno et al (2005) have shown that there can be spicules with magnetic fields as high as 40G.Intriguingly the value of the magnetic field in the quiet chromosphere has been estimated to be about 50-100G Andreas Lagg (2009). UV and EUV data have revealed explosive events in the transition region, but their relationship with spicules remains unclear. DePontieu(2007) advocates determining this

through a series of coordinated Hα and UV/EUV images to determine if the same spicules in Hα are also visible in UV/EUV images.

Energy transfer through spicules?

Spicules are energetic morphological features. The question frequently asked is what is the mode of transfer of energy in these events? To understand this, it is imperative to take a look at the various theories of energy transfer that have been proposed. Sterling (2000) observes that the use of computer simulations has brought in the use of numerical non-linear simulations to explain the development and evolution of spicules and consequently their method of energy deposition. There are three principal methods of the deposition of energy that have been isolated by these numerical methods: a) velocity or pressure applied to the spicule at its formation at the base of flux tube(this has been referred to as the 'toothpaste squeeze effect') and b) a pressure pulse released in a localized region in the flux tube in the middle or upper chromosphere and Alfvén waves generated by twists or disturbances at the base of the magnetic flux tube. The amount of energy needed to support a spicule is roughly estimated by Sterling(2000) to be about 10^{25}erg assuming a constant density. Foukal(1990) proves that there is enough energy granular motions to act as an energy source to spicules. Roudier et al.(1994) also believe that the ubiquity of granules makes them likely candidates for a source of energy for spicules. It's important to recognize the method of energy deposition is also closely related to how spicules are generated. It is presumed that the energy source for the spicules lies in the photosphere, though it is unclear exactly how the energy of the source is actually converted to spicule motion Sterling(2000). There is a conflict in the sense that if the standard assumptions are to be held regarding photospheric velocities etc and

radiation losses are ignored then spicule formation is explained through the rebound shock model. Sterling(2000)

This is related to the energy transfer using an acoustic gravity wave train which consists of a wavefront followed by an oscillating wake- upward along the flux tube. This wave propagates at the acoustic cut off frequency. Because of the abrupt drop off of the density in the chromosphere, conservation of kinetic energy necessitates that the wave amplitudes grow. Simulations have suggested that for this to occur the waves need to propagate in the form slow mode magnetohydrodynamic (MHD) shocks Sterling(2000).

Oscillations and energy transfer through the oscillations:

Another method of energy transfer is through oscillations in the chromosphere. A probable scenario is that the solar global oscillations could excite MHD waves in photosphere which may propagate through the chromosphere and which will then carry the relevant energy to the corona. The method of tracking these MHD waves is by observing the oscillatory nature of spicules.

The first Doppler shift in spicules suggesting that spicules could be oscillating was first noted by Nikolsky and Sazanov (1967). These oscillations consisted of both vertical as well as horizontal oscillations. Kulidzanishvili, V. I.; Zhugzhda, Iu. D. (1983) have looked at the same problem from a different perspective. They have given a theoretical reasoning for the transformation of vertical 5-minute oscillations into horizontal oscillations. Using previous results, they obtained Hα images of spicules at various heights “quasi-synchronously”. As the angle of motion differs so should the velocity component. Thus they conclude that there are some horizontal oscillations as well as vertical oscillations.

Weart (1970) noted that there was a significant input into the dynamics of the spicules because of their horizontal and vertical motions. In the same paper, though, Weart(1970) notes the lack of any statistical significance to the horizontal motion of spicules, implying that the horizontal motion was not of much physical relevance. Gadzhiev and Nikolsky (1982) later discovered that spicules oscillate both in the line of sight and tangential direction with approximately the same velocities. The same authors also concluded that the spicules undergo a form of cyclic motion with a period of 4 minutes and an amplitude of roughly 11 km/s. Papushev and Salakhutdinov (1994) found that the period was between 80 and 120 seconds. Kukhianidze et al. (2006); Zaqarashvili et al. (2007) suggest that the transverse oscillations of spicules occur by the action of kink waves or Alfven waves.

Based on these observations, it is generally construed that these oscillations, represent waves that propagate along the magnetic field tube from sunspots to the corona. Since the magnetic field tubes are anchored on the photosphere, it is suggested that the source of the waves lies in the photosphere. It is, therefore theorized, that the waves carry spicular material from the photosphere to the corona. The oscillations serve as the mechanical medium to carry the energy and momentum to the corona. Primarily three different kinds of methods have been isolated to guide the energy through the magnetic tubes: kink, sausage, and torsional Alfven waves as per Kukhianidze (2005). These waves may be observed by looking both at the Doppler shift oscillations and the time scales of propagation. The transverse oscillations observed by Kukhianidze (2005) on the solar limb are thought to be due to the propagation of kink waves. The sausage waves are known to cause oscillations mainly in the line intensity due to density variations. The

"squeezing the tube effect" is estimated to be caused primarily due to the presence of 3-4 photospheric granules in the vicinity of the base of the tube. It is not fully understood what kind of oscillations occur beneath the photosphere, and propagates them in the chromosphere. It is unclear whether it is standing waves beneath the chromosphere that causes the oscillations or it is due to propagating waves. Observing these oscillations in the photosphere would enable us to understand how these waves are characterized.

The logical order would be now to understand if these oscillations could be observed in the photosphere. De Pontieu,(2004), tried to correlate the oscillations on the photosphere with those in the chromosphere. De Pontieu (2004) starts with the problem statement that the oscillations in the corona are poorly understood and it is unknown whether this oscillation is related to the 5 minute oscillations in the Sun and it is important to investigate whether the photosphere oscillations can in some way be conveyed to the corona. De Pontieu (2004) compares the oscillations in the coronal loops right above sunspots that are very similar to the 3 minute oscillations in the photosphere. It is directly observed that non-sunspot regions have oscillations longer than 3 minutes, which begs the question if the coronal loop oscillations are related to the acoustic transmission within the Sun. Since the wave trains observed in the NOAA Active region 8558 are of finite durations, De Pontieu, (2004) performs a wavelet analysis on this region. Analysis of the observations, leads De Pontieu,(2004) to the conclusion that the Hα oscillations are caused by Doppler shifted features in the wings of the same frequency. This, according to Kukhianidze(2005),is partially due to longitudinal oscillations of the sausage waves.The important contributors, however, to this kind of oscillations is probably the kink waves according to Kukhianidze (2005).

The correlation with Extreme Ultraviolet (EUV) and Hα proves that the spicular jets obscure and interact with upper Transition Region (TR) plasma and transmit the EUV emissions. However, this information does not constrain the height of spicular structures. Thus with this correlation and previous observations the authors conclude a strong (quasi) periodic mass flow in the chromosphere observable on the limb propagating towards the corona. With this being true the standard life cycle of spicules, the authors conclude, would be 1-2 minutes where it reaches its maximum extent and then falls back to the Hα blue wing and then begins to appear in the red wing. This clearly proves that there is a general correspondence between mass flows in the chromosphere and transition region.

There seems to be evidence of these oscillations extending into the corona as well. It is well known that oscillating coronal loops are triggered by flares. De Pontieu et.al.(2005) specifically claims to provide evidence that the coronal oscillations are the same as the 5 minute oscillations in the photosphere and also suggests a relationship between chromospheric and transition region oscillations. De Pontieu et.al. (2005) suggest that chromospheric oscillations are caused by periodic upflows and downflows of material through the spicules. De Pontieu et.al. (2005) bring into picture that the spicules themselves are driven by p-modes from the chromosphere.

This is where the idea of a leaky chromosphere comes into picture. The idea is that much of the chromospheric spicular energy is leaked out from the spicules into the middle of the chromosphere. Though the p-modes , vanish within a short period of time, De Pontieu et.al.(2005) claims that previous research proves that they can leak significant amount of energy into the middle chromosphere, guided by rigid flux tubes inclined away

at an angle Θ from the vertical. The exponential decrease of density with height leads to a non-linear steepening of the tunnelled photospheric oscillations in the chromosphere so that magneto-acoustic shocks form and drive chromospheric plasma upward at velocities of 20km/s.

Ellerman Bombs

It is pertinent to review the properties of Ellerman Bombs(EBs) from the perspective of the dynamic chromosphere and their relation to the photosphere spatially. Ellerman bombs are Hα features, but they require a very fine resolution of greater than 0.17 arcseconds to be observed. The EBs are important features which are related to the magnetic reconnection events and appear within the photospheric intergranular lanes. A discussion into the EBs is warranted here to explain their overall properties and to highlight the usefulness of magnetogram data.

Vorpahl et al(1972) describes the differences between the Ellerman Bombs and other bright chromospheric features. These features are directly related to the positions of the Sunspots on the photosphere. Vorpahl et al(1972) reports the separation of the bright feature from the Sunspot pore and movement to another set of bright spots developing an emerging flux region. The relative separation rates were reported as 0.3 to 2 km/s. EBs are sometimes strangely visible on the central part of the Hα spectrum , however that seems to be rarity according to Vorpahl et al(1972) because the view of the EBs is mostly covered by darker chromospheric fibrils which fill up a larger volume of intense Hα emission in vertical fields. There is a less dramatic increase in brightness in the 3840Å band with an uncertainity of 1 or 2 minutes in the time at which maxima is reached. The lifetime of the bombs are reported to be between 7-64 minutes with the

median occurring at about 28 minutes Vorpahl et al (1972). The longest duration bombs are those in the regions where the most prominent emergent flux regions exist on the photosphere. This also corresponds to the intensity curves of the Ellerman bombs observed which seems to be the highest in the region that is most active.

Initial research in the 1970's was incapable of determining the polarities of EBs possibly due to the absence of magentogram data. The magnetogram was principally employed with the observation of the apparent relation between the development of the EBs and the appearance of a feature on the limb associated with the Sunspots in a wavelength of 3840 Å. The 3840 Å wavelength network of EBs was noted to have EB's typically around the area of emergent flux regions and in and around the regions of the sunspot penumbrae. The highest intensity EBs were typically observed to have the greatest intensity where the emergent flux regions were the most active. Another case of increasing intensity of the EBs was observed in the part of the photospheric chain of EBs consisting of opposite polarities of the same emergent flux region. These observations of the magnetic field were the results of magnetogram data.

Uncertainty exists on exactly how the magnetic fields of the sunspots affect the bombs. There is the view of Kitai(1983) suggesting that the bombs occur in isolated magnetic flux tubes, whereas Rust(1968) suggests that they lie above the magnetic reconnection neutral points. The EBs are reported to have velocities ranging from 0.6km/s to about 1-2 km/s(Nindos(1997)). Nindos(1997) studied the properties of EBs using the Big Bear Solar Observatory(BBSO). The Hα images were recorded approximately every 30 seconds while the magnetograms were recorded every 2.5 min. The bandwidth of the Hα filter was 0.25 Å. The goal of the study by Nindos(1997) was to

study the fainter and more diffuse EBs using a filtration technique to better reveal these features. The result of this analysis was that there were a set of EBs that did not correspond to definite magnetic elements and these were called class I EBs. These corresponded to about 64 % of all the bombs. The remaining were called class II EBs. Contrary to Bruzek(1972) who said that the lifetimes of the EBs were about 20 minutes, Nindos(1997) found that the maximum lifetime could not be more than 13.5 minutes. It is observed that the Class II EBs tended to be larger, marginally less bright and lived longer than the Class I EBs. The image of an EB surrounded by multiple tiny moving magnetic features is depicted in Figure 5

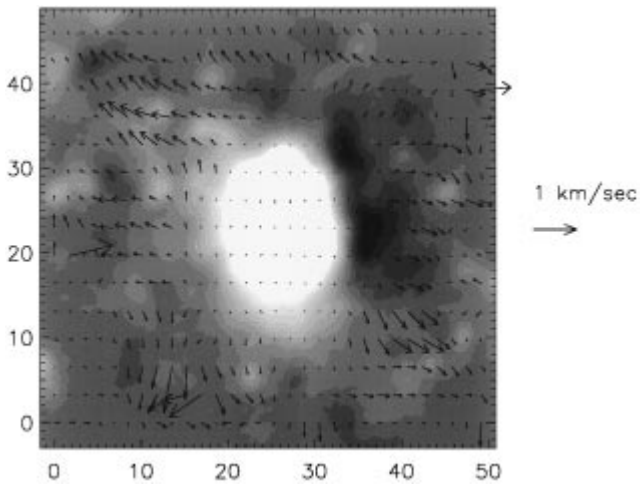

Figure 5: Moving Magnetic Features of an Ellerman Bombs: Flow map of horizontal proper motions derived from a time series of 36 magnetograms using local correlation tracking techniques. (Source Nindos(1997))

The moving magnetic features (MMFs) appear to be magnetically active areas around active regions which also tend to coexist with EBs in the vicinity of the sunspots. The inference from the image was that the moving MMFs tended to migrate towards the positive polarity. In most of the published papers on MMFs, they appear in positive-negative pairs, however occasionally the existence of unipolar MMFs with the same

polarity as the sunspot has been confirmed in decaying active regions (e.g., Zhang et al (1992)). Another set of results was that enormous EB s are triggered at the edges of supergranular boundaries and are mostly short lived, their locii also, do not travel very large distances. Thus EBs are examples of solar features where the observational data from space crafts and magnetograms has yielded a wealth of information on their physical properties Nindos(1997).

Properties of Plages

It is important to understand plages from the perspective of the dynamic chromosphere. One of the most important observations mentioned by Shine and Linsky (1974) is that the primary resonance lines of Ca_{II}, H and K where plages are visible and are generated by collision-dominated initial source functions. Thomas and Athay(1961) , Dumont(1967) and others have concluded that the reason for the existence of plages is the increase in chromospheric temperature, the temperature gradient, the electron density, a decrease in the micro-turbulence relative to the quiet chromosphere or some combination of these factors. Whereas Zirin(1961) and Pasachoff et al (1968) have interpreted the presence of H and K lines as a combination of the small scale features which have simple absorption or emission features moving relative to each other. However, high resolution studies very clearly indicate that this kind of an interpretation is inadequate, especially when one takes into account the center-to-limb behavior. The center-to-limb behavioral difference is primarily due to the inability to reproduce results in high resolution while making simultaneous on-disk and limb measurements (Shine (1974)).

Some of the elements observed in the plages seem to be complementary to one another, Liu and Sheeley (1971) reports that whilst the CN spectrum reveals fine features,

it is the violet emission peak(K_{2v}) of the 3934 Ca_{II} that reveals the fine network structure of the plages in the chromosphere. The elements in the spectrum appear to range from 1500km to several thousand kilometers, correspondingly the CN spectrograms reveals that these features have dimensions which are close to about 1000 km. The CN network itself is fluctuating and variable, not too different from the background CN itself. This is apparent in the Figure 6 below

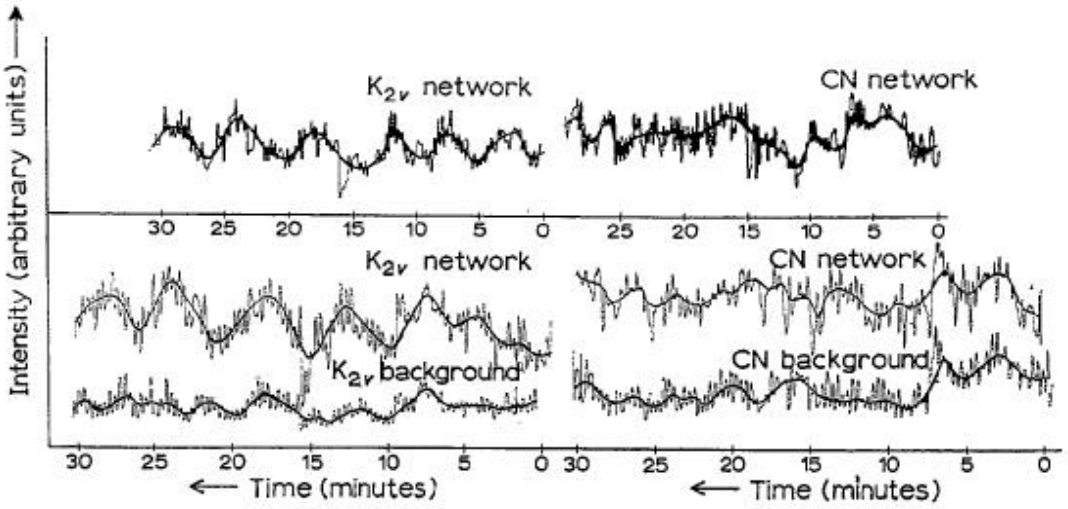

Figure 6 CN and K_{2v} background radiation: Plots illustrating the different intensity variations of simultaneous CN and K_{2v} network fragments with time. (Source: Liu and Sheeley (1971)

Many investigators have speculated that the cause of increase in emissions in plage regions is a doubly reversed non-Linear Thermodynamic Equilibrium (LTE) source function. Shine (1972) advocate the use of the column mass as a function of temperature because the value of this mass does not vary greatly over optical depth and therefore is more useful in adjusting temperature. The authors reproduce the apparent rise in pressure

at about 8300K which is the vicinity of the temperature minimum as shown in Figure7

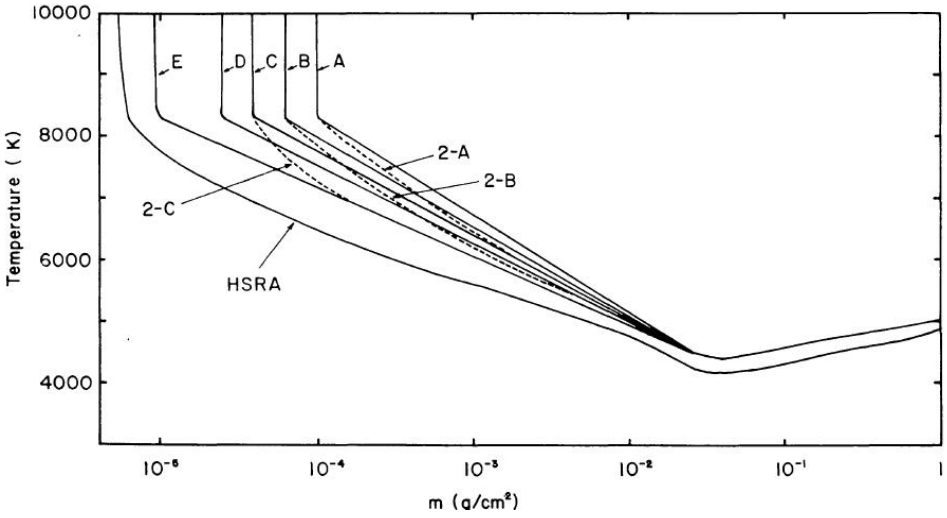

Figure 7: Temperature-Mass distributions: The figure indicates the distribution of mass and temperature variance in linear vs concave plages. (Source:Shine(1972))

The question then arises; are plages are magnetically active at all? (Ishikawa & TSuneta, 2008) raise the pertinent question of whether the transient magnetic fields observed in the plages are a function of the global magnetic dynamo of the Sun or whether this is a function of the physics of the plage itself. The primary magnetic field signatures of the plage and the quiet Sun regions are very similar (Centeno et al. 2007; Ishikawa et al. 2008), so it's a challenge to determine the true cause of the magnetic fields. The magnetic fields are also very hard to study because the plages, as previously noted, are normally formed in the vicinity of Sunspots which emit complicated and very convoluted fibrils and tubes; therefore one of the methods of studying the magnetic fields in plages is by observing the p-modes propagation within them. The incoming acoustic waves interact with the magnetic flux tube, exciting sausage and kink tube waves which propagate downward and upward carrying away energy, thereby producing absorption. Some of these techniques have been used by Braun and Birch (2008) who use what is known as the ridge technique to analyze p-modes. Braun and Birch(2008) note that the

plages themselves absorb acoustic energy with a broad frequency range centered at roughly 3.5 mHz and with a width of 1 mHz. Some of the assumptions made in the prediction of the magnetic model of the plages are :

- The solar photosphere consists of many thin vertical, magnetic flux tubes embedded in a field-free polytropic atmosphere.
- The field-free atmosphere supports f - and p-mode oscillations that interact with the magnetic flux tubes, exciting longitudinal and transverse oscillations in the form of sausage and kink tube waves.

These waves propagate up and down the flux tubes carrying away energy from the f and p modes, thereby damping the modes. This decrease in energy, apart from depending on the nature of the incoming wave, also depends on properties of the flux tube such as plasma β and cross sectional area which are defined in Jain et al(2008).

Flares in the chromosphere

It is worthwhile to consider how solar flares affect the chromosphere. Ricchiazzi and Canfield (1983) have presented a steady state calculation of chromospheric response to non thermal electrons, enhanced thermal conduction and enhanced gas pressure from the corona. The general idea is to set the theoretical limits to the energy spectrum of the non-thermal electrons present in the chromosphere during flares. Earlier work on this did not include the radiative losses in Ca_{II} and Mg_{II}, radiators which could dominate the hydrogen loss rate. Typically the emission streaks left by flares in the chromosphere, visible in the Hα are called Red Streaks by Ichimoto et al(1983). These red streaks are typically characterized by spatially confined small flare points successively brightening

in the Hα flare kernels which may be identified with footprints of flaring loops in the photosphere. These red streaks/flashes are important as they reveal the thermodynamic structures in the chromosphere. These red flashes were observed almost always present in all flares right at the beginning of the flare itself. A typical red assymetric flash is as shown below

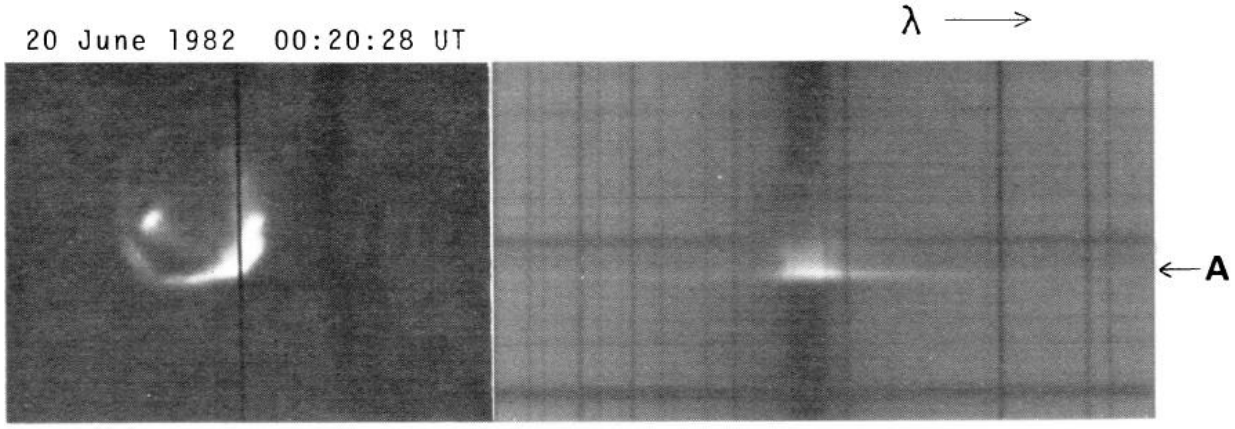

Figure 8: Red Assymetric flash The region marked A here shows the flash in spectrum and the left side of the palette shows the Hα image (Source Ichimoto et al(1983))

The region marked A in the Figure 8 is the region of the chromosphere where the flash was observed. The most probable explanation by Ichimoto et al(1983) for red assymmetry is the downward motion of material in the flare emitting region. Conspicuous downward velocity of the flare emitting region was found to be about 40-100km/s. These motions seem to dynamically become more active at the onset of the flare and reach maximum velocities a little before the peak at microwave frequencies.

Chromospheric evaporation and the eventual condensation of the material is another physical process associated with effects of flares on the chromosphere. The post flare loops in the chromosphere produce drastic mass motions by rapid energy transport caused by non-thermal or thermal conduction. For energy fluxes of the order of 10^{10} ergs

/cm^2/s^1 (Li and Ding (2011))the evaporating plasma flows at several tens of kilometers upwards from the chromosphere with no notable downflows(Li and Ding (2011). This is termed as 'gentle evaporation'. Evidence of gentle evaporation was also presented by Brosius & Phillips (2004) during flare precursor events and by Singh et al. (2005) during coronal loop formation, but in these cases the mechanism(s) responsible could not be verified. However any non-thermal evaporation does not have any observational evidence during the impulsive phase of the flare. It was noted that at high non-thermal fluxes, the chromosphere is unable to radiate at a fast enough rate and consequently expands rapidly. According to Milligan et al(2006) the heated chromospheric plasma at approximately 10^7 K expands upward at hundreds of kilometers per second in a process known as "explosive" evaporation. The overpressure of the flare plasma relative to the underlying chromosphere also causes cooler, denser material to expand downward at tens of kilometers per second producing an effect known as "chromospheric condensation".

Milligan et al(2006) have used the data from Ramaty High Energy Solar Spectroscopic Imager (RHESSI) to do their investigations on the chromospheric evaporation. The data contains simultaneous X-ray and Extreme Ultraviolet observations of gentle chromospheric evaporation. Previously it was assumed that these evaporations had a rate of about 80 Km/s but Milligan et al(2006) clearly demarcate different evaporation rates for different ionizations of various elements. Upflows of the order of 13±16, 16±17 and 110±58 Km/s were observed for He_I ,O_V and Fe_{XIX} respectively. Milligan et al(2006) feel that further additions of EIS observations with the RHESSI data would give a much better understanding of these evaporations.

Chapter III. Instrument Description

Internet Observatory #2

This thesis has been conducted at University of North Dakota (UND) Observatory located near Emerado, North Dakota. This is approximately 10 miles west of the main university campus. The latitude and longitude of the observatory are 47.919° N, 97.331° W respectively. The physical address of the observatory is 1652 23rd St NE Emerado, ND 58228.

The observatory mission is best explained by the mission statement on the observatory website http://observatory.space.edu

"The primary objectives that the UND Observatory pursues to accomplish its mission include: 1) maintaining and operating a multi-telescope, multi-wavelength facility for the conduct of research and education projects; 2) conducting complementary research projects that assist research programs at the larger national observatories, 3) offer research and education opportunities for the study of asteroids, variable stars, and the Sun, and 4) promoting science, technology, engineering, and mathematics (STEM) education in North Dakota's colleges and K-12 schools." [http://observatory.space.edu]

The capabilities developed in this thesis also have the mission of establishing complementary research projects that assist research programs at larger observatories. This thesis intends to lay the groundwork to develop the capability to continuously monitor the Sun under the aegis of the UND Observatory which is part of the UND Department of Space Studies. The observatory consists of three independent Internet

controllable telescopes: Internet Observatory #1(IO1), Internet Observatory #2(IO2) and Internet Observatory #3(IO3). Each telescope is housed in a roll off roof structure and has a dedicated computer that is used to control the telescope and acquire CCD images. The telescopes of IO1 and IO3 have similar capabilities and are currently dedicated to nighttime observing. This thesis uses IO2 as the primary telescope of operation to observe the Sun.

Software and resources

IO2 consists of a Windows ©7 PC which runs MaximDL© to control the telescope and camera. Accurate tracking is achieved with the Meade LX200GPS mount. The computer is temperature regulated with an air-conditioner in a box that provides cooling, heating and filtering to protect the computer from the external environment. The IO2 is erected in a roll off roof structure shown in Figure 9.

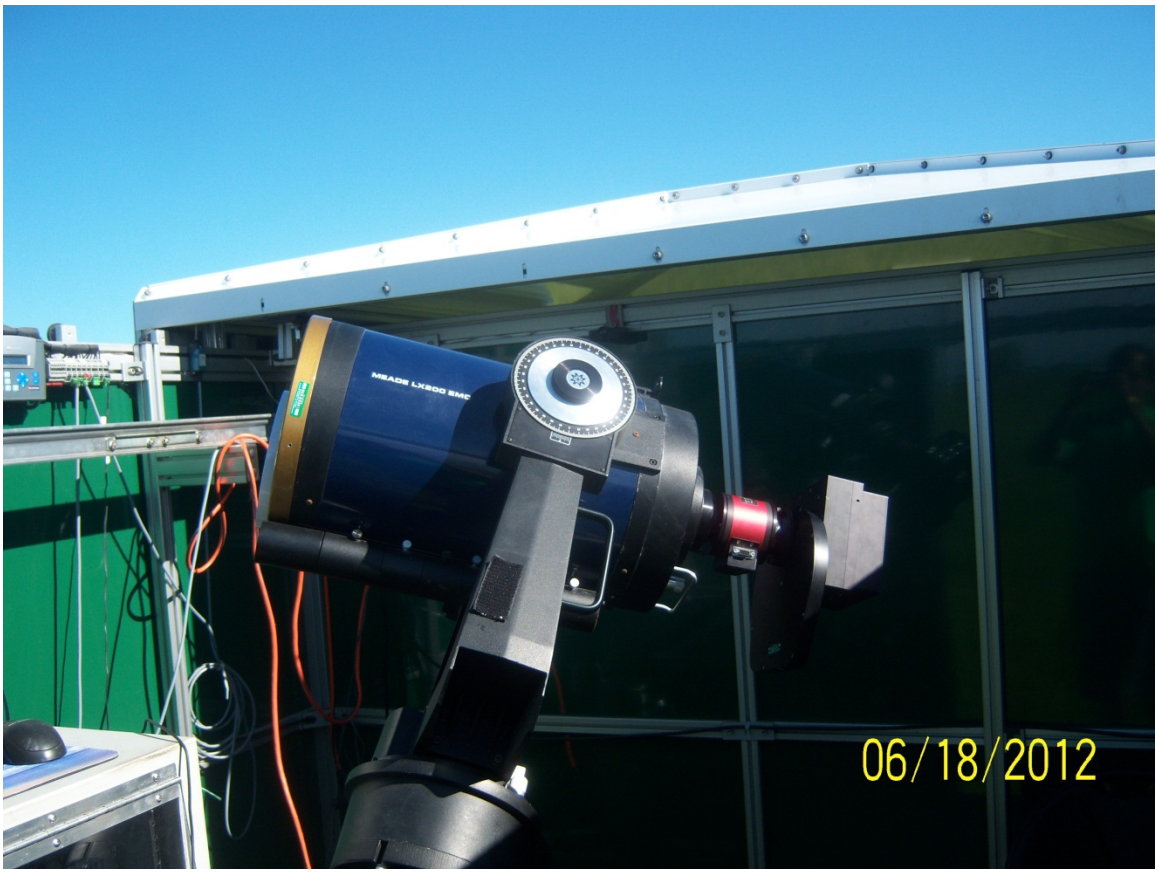

Figure 9: Internet observatory #2 mounted with the Energy Rejection Filter (ERF), Daystar 0.4 Å Quantum Hα filter, interference eliminator, ND filter and the Finger Lakes Instrumentation (FLI) 4096 x 4096 CCD camera

The roll off roof can be closed when the telescope is not operational. At this time the Daystar Hα filter, CCD camera/filter wheel are removed and placed within the observatory trailer that offers a temperature controlled environment. The IO2 also has the capability to be accessed remotely through a local wireless network that is connected to the UND Aerospace computer network.

A. DayStar Quantum H-alpha filter

Hα observations, for this thesis, at the UND Observatory have been achieved using a DayStar Quantum 0.4Å Hα filter. The filter type used for this thesis is the Quantum

Professional Edition (PE) hereon referred to simply as Quantum. The filter is unique in its line of filters in the bandwidth that it offers and the range of applications it supports; ranging from space-based to ground-based solar observations. The filter relies on the Fabry-Perot etalon design to do the appropriate filtering of the sunlight. It is usually used in conjunction with a heliostat or in the optical path of the telescope. This thesis makes use of the latter method and places the filter at the back of a Schmidt Cassegrain design optical telescope (SCT). The typical bands that the Quantum band pass filter looks at is Hα, Calcium II-K line, sodium D line, Helium D3 line, Hβ etc. The bandpass filter is designed to block all other light except the narrow band wavelength emitted or absorbed by the desired element under study. The Hydrogen alpha (Hα) wavelength, used in this thesis, is centered at 6562.8Å. This is used primarily in chromospheric, disk and limb, observations. The Quantum can be applied either before or after the light path enters the telescope. The position of the placement of the Quantum depends on what kind of application the filter is being used for. For this particular thesis goal, where the resolution is limited by atmospheric seeing, the filter needs to be placed in the path of a concentrated beam of light to ensure that highest quality focus and the best visibility of features. Therefore, for this thesis, the Quantum has been placed at the back of the SCT. This also offers the flexibility of being able to port the entire set up to a telescope of a different aperture.

Central wavelength and frequency of operation

The Hα line lies at 6562.8 Å in the visible spectrum towards the red end of the spectrum. The Hα line corresponds to the chromosphere and chromospheric features such as prominences. The line consists of both absorption as well as emission spectra.

The on disk features in Hα are cooler absorption features whereas the limb features such as prominences are emission features. These features are best observed with a narrow band Hα line. The Quantum offers an extremely narrow band Hα line. A standard absorption feature is shown in the Full Width Half Maximum (FWHM) Figure 10. The FWHM is the bandwidth of the filter where the transmission or absorption of the band is 50%. A smaller FWHM will thus imply a narrow band width.

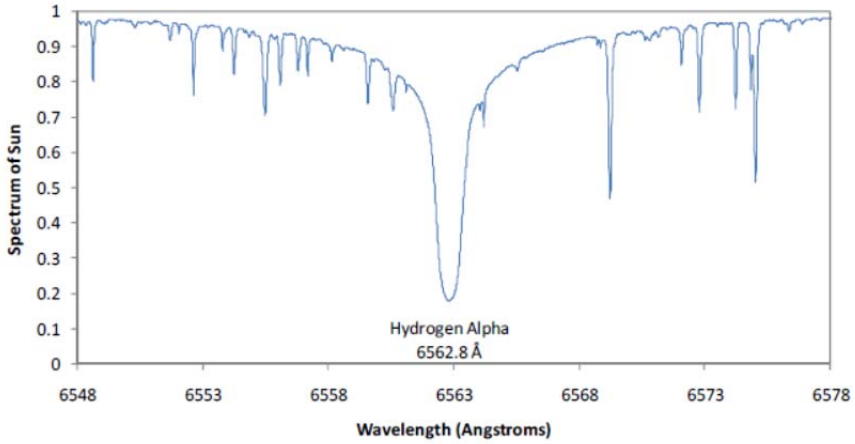

Figure 10: H-alpha spectrum. A standard Hα absorption feature represented in the Daystar manual Source Daystar Filters (2009)

The reason for the typically narrow bandwidth for the Hα filter bandwidths is that most absorption features in this wavelength have bandwidth of 0.8 Å. The narrower this bandwidth is the greater is the effective contrast in the observed feature with the exclusion of continuum and Doppler shifted light. However, while this is true in general, each feature has its own specific bandwidth for observation. In order to see really fine features one needs an extremely narrow bandwidth. The most obvious detail that can be observed with a bandwidth of 1.0 Å is prominence detail. To observe prominence detail and spicules, a bandwidth of 0.7 Å or lesser is recommended by Daystar Filters(2009). The chromospheric network needs a low bandwidth of 0.4 Å. This is the bandwidth that Quantum offers. There is a provision within the filter where the Central Wavelength

(CWL) can be blue shifted or red shifted towards the blue or red wing to observe velocity of material moving towards and away from the line of sight observations. The Quantum offers ± 1 Å wing shift range.

Physical construction and parameters

The Quantum is constructed as a Fabry-Perot etalon with high finesse and low fringing that exhibits multiple high transmission peaks in successive orders with a FWHM of 0.4 Å. The finesse is a filter property that defines the reflectivity of the filter stack and the fringing is a filter defect that is a result of interference. The filter itself is a stack of multi-layered etalons with various components. The glass used for the external coating is ¼ wave or better, anti-reflection (AR) coated BK7 glass. To achieve the narrow bandwidths exhibited, multiple etalons with high precision are stacked.

The CWL is a function of the principle of operation of the filter. This draws back to the theory of how a Fabry-Perot etalon works. It is essential therefore to briefly describe the working of an etalon.

Principle of operation of an etalon:

A Fabry-Perot etalon works on the principle of interference of multiple light rays reflecting off a highly reflective surface such as a silvered mirror. The central wavelength of light that this setup generates is given by the equation:

$$\lambda = 2\eta l \cos(\theta) \quad \text{.....(1)}$$

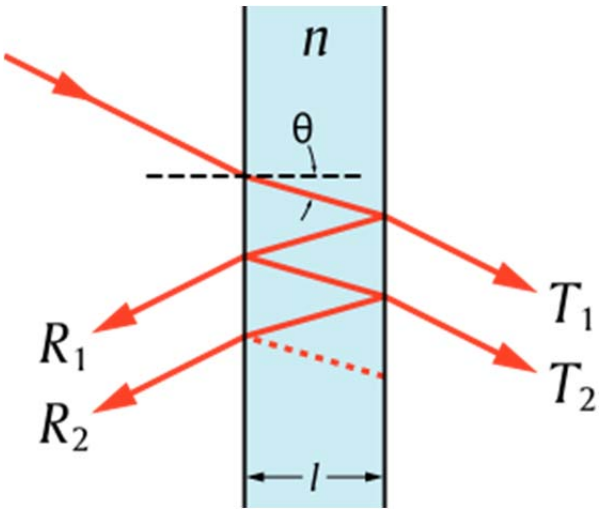

Figure 11: Construction of an etalon where: *l* represents the distance between the mirrors, θ represents the angle of incidence of the incoming light, and η represents the refractive index of the medium between the etalon plates.

The wavelength, λ, is a result of two rays being incident at an angle θ and interfering constructively with each other and producing a central wavelength peak at the wavelength λ. For this it is necessary that the reflectivity of the etalon be very high so that the reflecting beams are in phase to interfere constructively. The constructive interference will result in a narrow FWHM of 0.4 Å. Therefore this reflectivity will also directly correspond to the accuracy of the central wavelength. Therefore to have an extremely narrow band filter, the reflectivity has to be sufficiently high.

There are a number of ways of slightly varying the central wavelength. Bland and Tully (1989) suggests a number of techniques, which include varying any one of the parameters in Equation 1 to get a shift in the central wavelength.

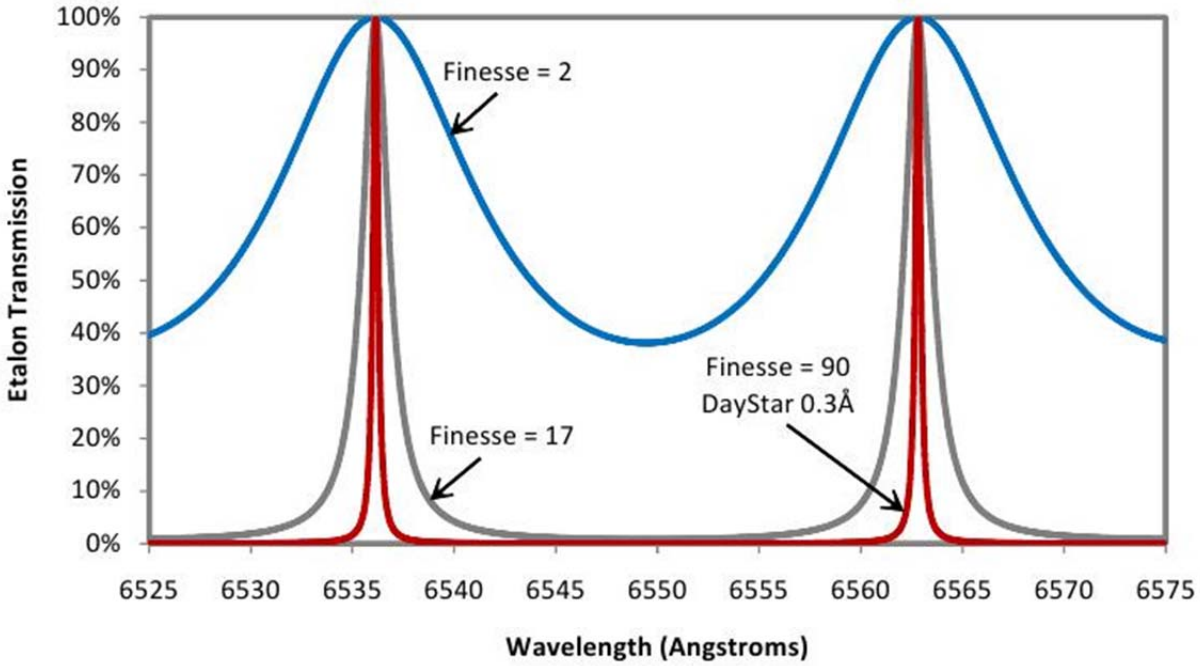

Figure 12: Finesse to FWHM relation, the plot shows how FWHM decreases, making the filter narrow band, with increase in Finesse.

The Quantum was manufactured with a finesse of 55. The FWHM of a small bandwidth Hα filter is shown in Figure 13

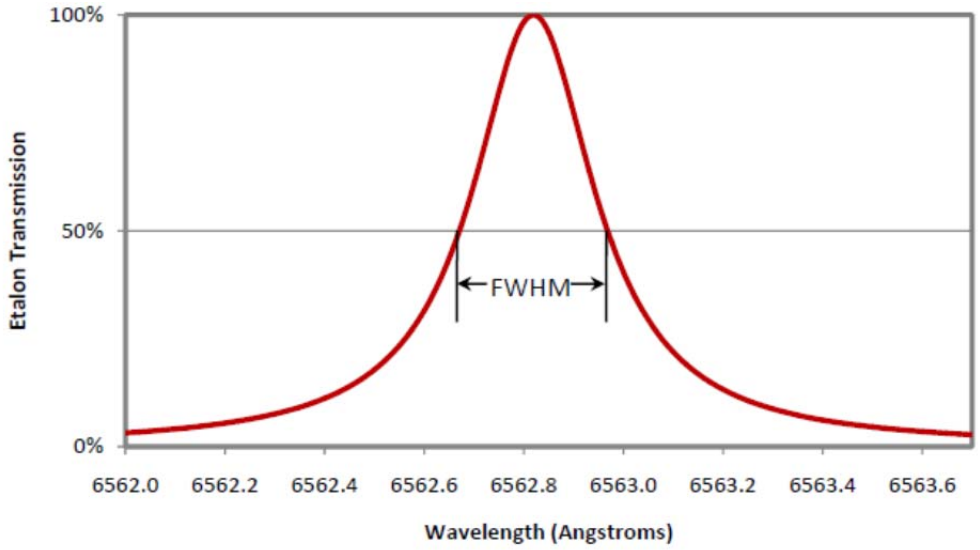

Figure 13: Transmission profile. A typical etalon transmission profile for the Hα feature. This figure indicates an ~0.35Å bandwidth filter. This is not the bandwidth of the filter used in this thesis, but represents a typical narrow band filter. Source: Daystar Filters(2009)

Figure 13 clearly indicates the amount of transmission that the filter will achieve based on the wavelength. The Quantum is designed to have maximum transmittance at the CWL at 6562.8 Å.

Dependencies of the CWL

The CWL aims to be stable for variations in any kind of environmental and equipment factors such as temperature and angle of tilt. However there are environmental factors that need to be compensated for in order for the filter to be stable.

Temperature: The CWL is sensitive to temperature and change in the tilt of the equipment. The reason it is sensitive to these two factors is the principle of operation which is dependent on the distance between the two silvered surfaces of the etalon. The peak transmission wavelength changes with changing distance between reflective sides due to the expansion or contraction of the mica caused by the change in temperature. Therefore the change in temperature has to be compensated (via a heater) with a radiating of energy through the Quantum. The change in CWL with the change in temperature is 1 Å per 17°F. The Quantum compensates for this by re-radiating the heat through the body of the filter. The Quantum has an aluminum ring surrounding the optical stack to maintain a constant temperature. As the glass itself is a poor conductor of heat, the heat will be radiated through the entire optical stack. The filter has to initially warm up to a constant temperature. Therefore, the face plate indicates an orange light while it's warming up and a green light when the optimum temperature has been reached.

Just like temperature the peak transmission wavelength will also change if there is a change in the angle of incident light. This is due to the change in the path length of the incident light from Eq (1). The change in the transmission wavelength is shown in the plot of Figure 14:

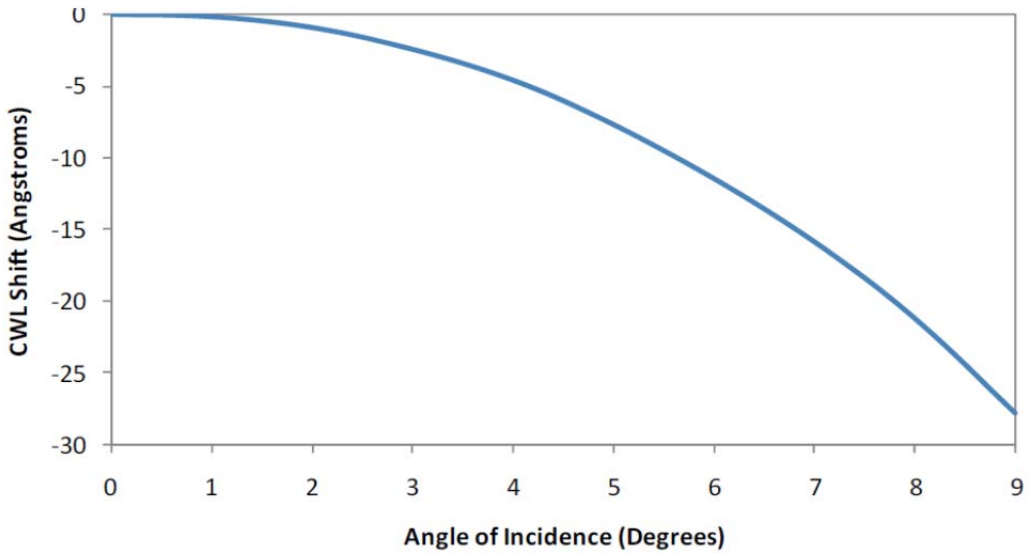

Figure 14: Tilt dependence of the filter. Change in CWL with change in angle of incidence of the light. Daystar Filters (2009).

This tilt dependence eventually leads to a cumulative widening of the FWHM. The change in the angle of incidence with light cone implies that for a zero shift in CWL the angle of incidence should be 0 with respect to the light cone. However, Figure 14 indicates a tolerance of tilt by about 1°. The change in the CWL with tilt has been modeled at 2*tan(1°) therefore the optical cone need to be within *f*/28 for bandpass applications to be within 1 Å. This thesis uses a bandwidth of 0.4 Å, so the focal ratio is placed higher at *f*/30.

The lower the bandwidth the larger the focal ratio needs to be in order to ensure that the center of the light cone has the incident focused beam of light. A plot of this is shown in Figure 15 below

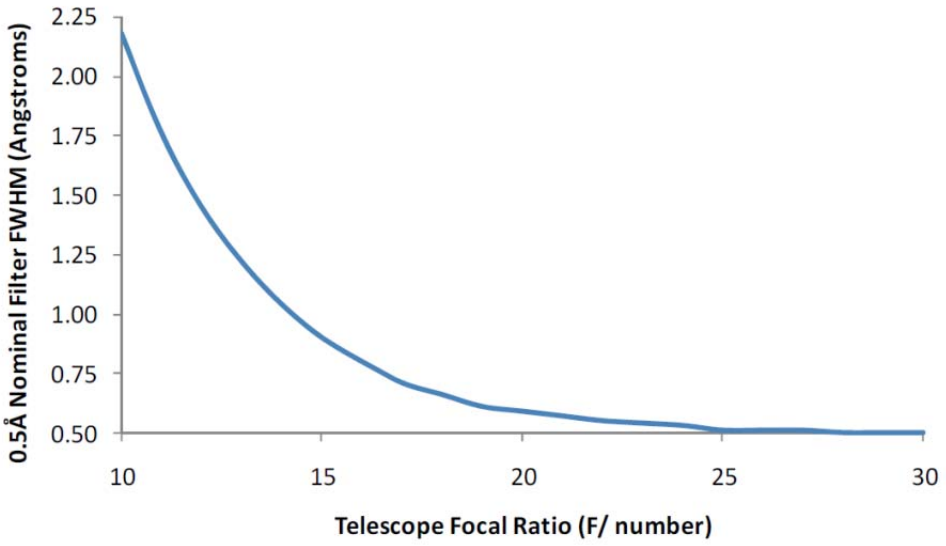

Figure 15: Optimal focal ratio. Optimal focal ratio for low bandwidth applications changes with central bandwidth. Daystar Filters (2009)

Construction and physical design

The construction of the Quantum etalons uses layered mica. Mica wafers are cleaved by hand and then laid out into parallel sheets. The method of refraction is achieved by changing element concentrations across the sample. This is, however, fixed after construction and cannot be altered by the observer.

The finesse and fine tuning of the CWL is done by coating these mica sheets with reflective and anti-reflective coatings alternately. The mica crystals themselves are seated in a high temperature rated optical couplant, in ¼ wave BK7 optical windows. Once this seating is achieved the whole assembly is sealed into place permanently within the

housing. The mica wafers sealed in this way cannot be separated without damaging the wafers. Therefore, there is no way to alter any internal properties of the Quantum without violating the filter.

Varying the temperature to go between the red and the blue wings of the spectrum is possible using the temperature sensor on the digital faceplate of the Quantum. The temperature sensor also ensures that the Quantum is at the CWL based on the temperature of the filter stack. As the filter cools off through the external aluminum ring the LED on the faceplate glows orange until the filter stack reaches the optimum temperature at which point it turns green indicating that the Quantum has reached optimum temperature.

Application and usage

There are primarily two ways in which the Quantum can be used while imaging. This typically depends on what kind of imaging is being done, whether the imaging is to do scientific imaging from large apertures or to do narrowband imaging to extract scientific data using smaller apertures. Based on this classification, the two kinds of imaging applications possible are

a) Pupil plane imaging: This kind of imaging is involves placing the filter in front of the objective, where the filter limits the light entering it, which the telescopic optics then focus and collimate to an appropriate focal length for observations. The CWL tuning and wavefront accuracy have to be more stringent for this kind of an application.
b) Focal plane imaging: This thesis uses the focal plane imaging method where the filter is placed behind the primary telescope objective lens or mirror of the

telescope. This method of imaging requires a very long focal ratio of *f*/28 or higher. The setup for this thesis has a recommended focal ratio of *f*/30 for the low bandwidth of the Quantum of 0.4 Å.

Additionally for the setup in Internet Observatory #2, since it is an SCT, the Quantum needs a wedge plate that is angled at 1.2° to the vertical plane. Figure 16 shows the filter attached to the CCD and filter wheel.

Figure 16 Daystar Quantum PE filter attached to the filter wheel and Finger Lakes Instrumentation CCD camera.

The Quantum has two exposed ends to it as shown in the figure. The end towards the blue button of the face plate has a red coating which is connected as shown to the filter wheel and the CCD camera. The other end has a yellow coating that

faces towards the direction of the Sun. The Quantum's temperature sensor is powered by an external power supply of 12 V DC.

B. 10" SCT LX200GPS Meade

This section of the chapter on instruments will focus on the elements of the telescope that are used to a) Find the sun b) track the sun and c) interface with the computer. While there is no need to delve into the theory of how a SCT works it might be worthwhile to have brief about what an SCT is and how it differs from a refractor which is probably the most standard light gathering apparatus in low apertures for solar observing. Figure 17 shows the non-scaled optical components of an SCT.

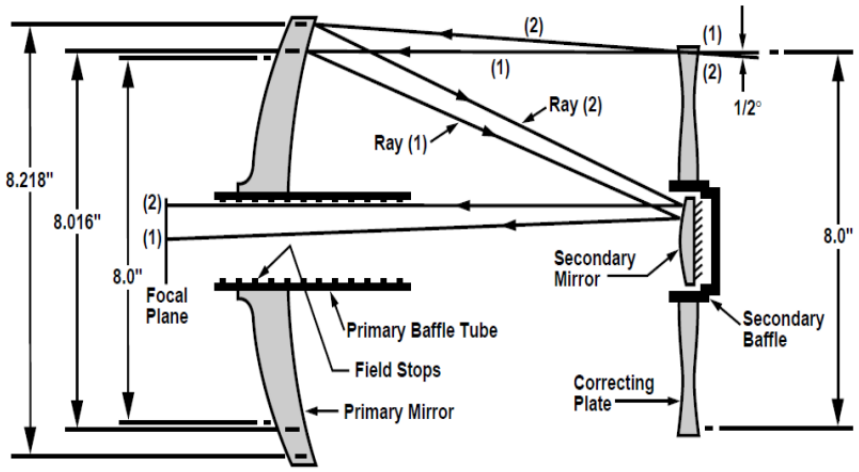

Figure 17: Construction of a standard SCT design with the ray diagram with the ray diagram Meade Instruments Corporation (2003)

Design and working of an SCT:

Standard SCTs are catadioptric designs where both lenses and mirrors are used in the light path. As shown in Figure 17, the light collecting mechanism is the same design as a reflector with the primary mirror acting as light gathering aperture. The secondary mirror is a convex reflector which focuses the light reflected by the primary mirror onto a hole in the primary mirror as show in Figure 17 where rays 1 and 2 converge. The corrector plate is a lens that corrects the incoming light for spherical aberrations.

Solar observations utilize an energy rejection filter (ERF) that covers the corrector plate at the end of the SCT optical tube. The ERF achieves two goals a) to reduce the amount of light incident on the objective and b) to achieve the large focal length necessary to maintain a narrow light cone to prevent any deviations of the CWL. The other optical elements for this thesis work out of the box, and there is no tinkering with the optical elements for day time observing. The objective is the end of the mirror cell at the left of the Figure 17 where the light exits onto the focal plane. The focal plane is where the filter and the subsequent CCD camera are placed. Hence the term focal plane imaging. The focal point of the incident light can be altered by changing the focal length minutely so as to achieve a sharp focus. There is a coarse focuser screw on the optical tube assembly for this focus adjustment.

Telescope data

The telescope has a published focal length of 2540 mm. The unstopped diameter of the aperture is 10 inches or 254 mm. This is stopped down to about 3.14 inches or 80 mm, providing a focal ratio of *f*/32.

C. ProLine PL16803 CCD Camera

Imaging is conducted using a ProLine PL16803 CCD camera. The physical specifications of the camera are shown in figure 18. The camera is externally powered with a 12V adapter. Like standard scientific CCD cameras, the one used for this thesis, does not have any lens systems. The light therefore is directly incident on the chip. The CCD is designed to operate to a temperature of 60°C below ambient temperature. The download data speed varies from1-8 MHz. For lower integration times the higher rate of download ensures that the images can be read out of the pixels immediately at the end of the integration time.

The total array size is 4096 x4096 pixels. The size of each pixel is 9 μmx9 μm. Therefore the plate scale of the CCD is calculated using the formula

Plate scale = 206265 *Pixel size/Focal length…… (2)

= 206265 *$9x10^{-6}$/2.54 arcseconds/pixel

= 0.73”/pixel

The total field of view for the CCD array is 49.89’x 49.89. This is the field of view that is large enough to fit the entire Sun which has a diameter of 31’.

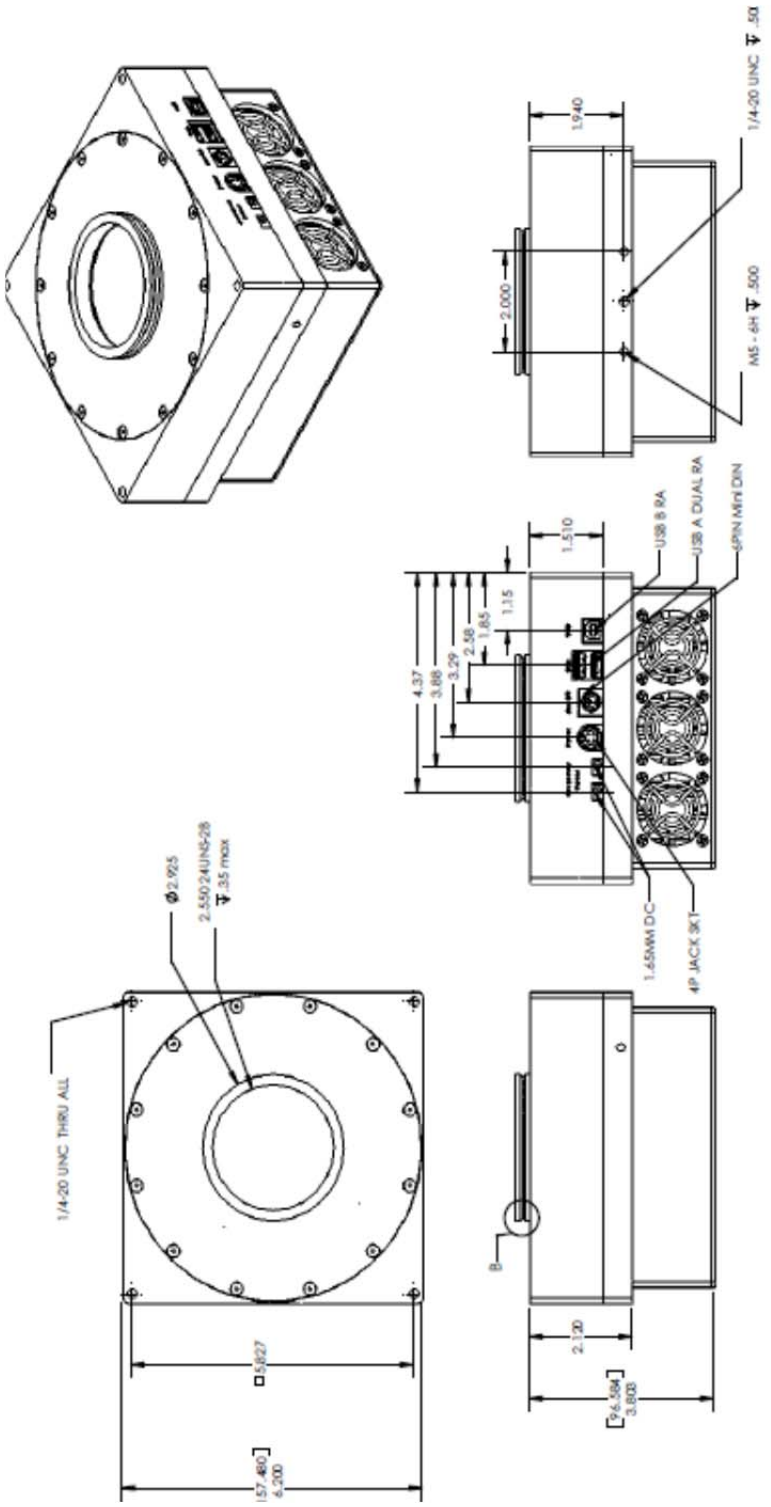

Figure 18: Dimensions of the CCD camera. The dimensions are in inches. Finger Lakes Instrumentation (2006)

Figure 19 is the representation of the efficiency of the CCD with varying wavelengths.

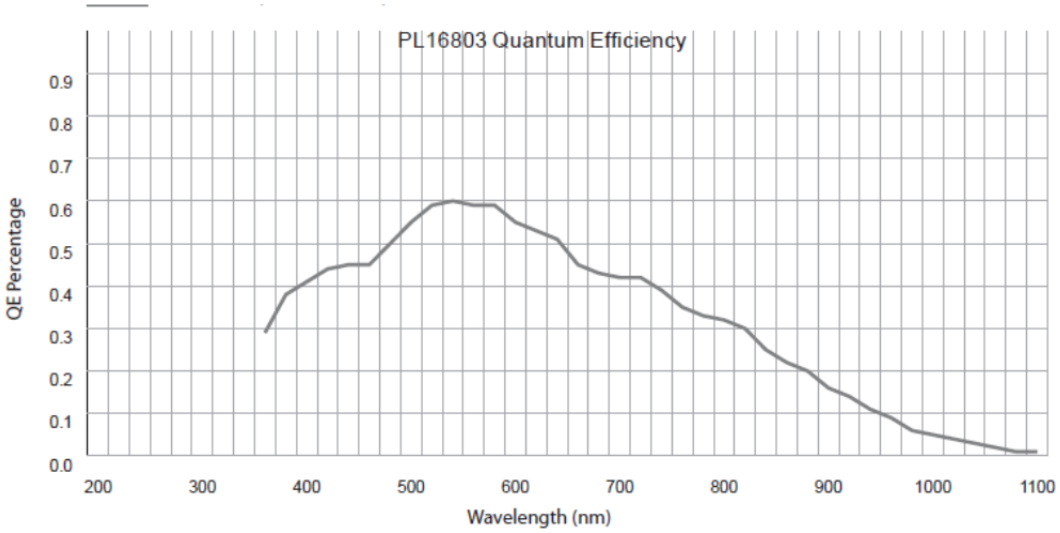

Figure 19: Quantum efficiency of the PL16803. Finger Lakes Instrumentation (2006)

The quantum efficiency is principally a quantity that measures the total number of photons that is detected by the CCD. This is however dependant on the wavelength, so that the sensitivity of the chip varies for different wavelengths. Therefore this is a measure of the sensitivity variation of the chip with change in wavelength of the photons received by the CCD.

The operating temperature is important to reduce the dark current and to maintain a stable linearity range. The non-linearity of the CCD occurs when the number of counts received by the chip goes above 40,000 but stays within 1% from the standard curve. The CCD chip used in the PL16803 is the Kodak KAF-16803 front illuminated monochrome chip.

CCD Response curve

The CCD response curve in Figure 20 shows the change in response of the CCD with changing exposure times. For obtaining this curve, the CCD aperture was covered with white paper to generate a uniformly illuminated surface. This was then covered with

layers of cloth to prevent stray light entering the CCD and produce excessive illumination because of the background light. Then small increments to exposure times were made to see the response and illumination of pixels at different exposure times. This was continued till the counts went up to 63,000 counts which is the saturation value of the pixels.

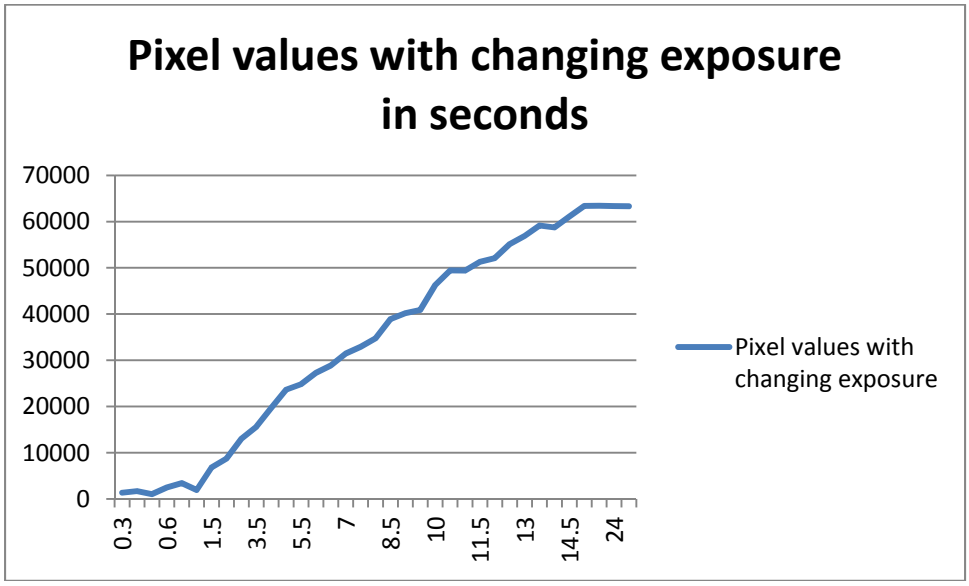

Figure 20 : CCD pixel values for changing exposure values. The y-axis indicates the pixel values for different exposure times. The x-axis is the exposure time in seconds.

The Figure 20 is the change in counts with increasing exposure time. The non linearity in the plot occurs at over 40000 counts, the graph after this shows non linearity in that it is no longer a straight line and the slope is variable. The interesting observation in this plot is the non-standard response to exposures lower than 1s. The author believes this might be an error in data collection as the CCD published characteristics does not suggest that this should happen.

D.Energy Rejection Filter (ERF)

Energy rejection is probably the most important aspect of observing the Sun. The high energy incident on a solar filter with a long focal length has to be necessarily stopped down with a band stop filter like an ERF. The ERF absorbs both heat and light. While the primary optical issues with excess light is one of over exposure and damage to the telescope's objective mirror and internal structure, the primary issue is one of how much energy is funneled into the Daystar filter. The ERF, by being designed to absorb energy, limits not only the excess light but also limits the amount of heat that is passed through the system. Heat is an issue with multiple components being connected and even with the optical system itself. Large amounts of excess heat, for a long duration can cause the optical elements to expand and crack. Heat is known to melt adhesive elements, damage couplings, and evaporate optical coolants causing indirect damage to the equipment. This issue becomes more intense when the beam is focused.

The ERF therefore plays a very important role and is a required optical component that is used with the Daystar Hα filters. The author has personally observed that when imaging through the day, the ERF becomes heated and the heat which can both be felt and observed in the expansion of the ERF. The ERF used for this thesis is shown in Figure 21

Figure 21: ERF. ERF used for this thesis obtained from Daystar with an aperture of 80mm

The red colored glass is an optical window which prevents the light below 6000Å passing through the filter. This kind of glass used in the ERF makes it incumbent to use the ERF in the front of the optical path as the glass is not designed for a concentrated, focused beam of light. The glass also makes it incumbent to do imaging at wavelengths above 6000 Å.

The critical aspect of this sort of an ERF is the point that they reject the energy by absorbing it as opposed to dielectric filters which reject by reflecting. The rejection curves of various ERFs is shown in Figure 22

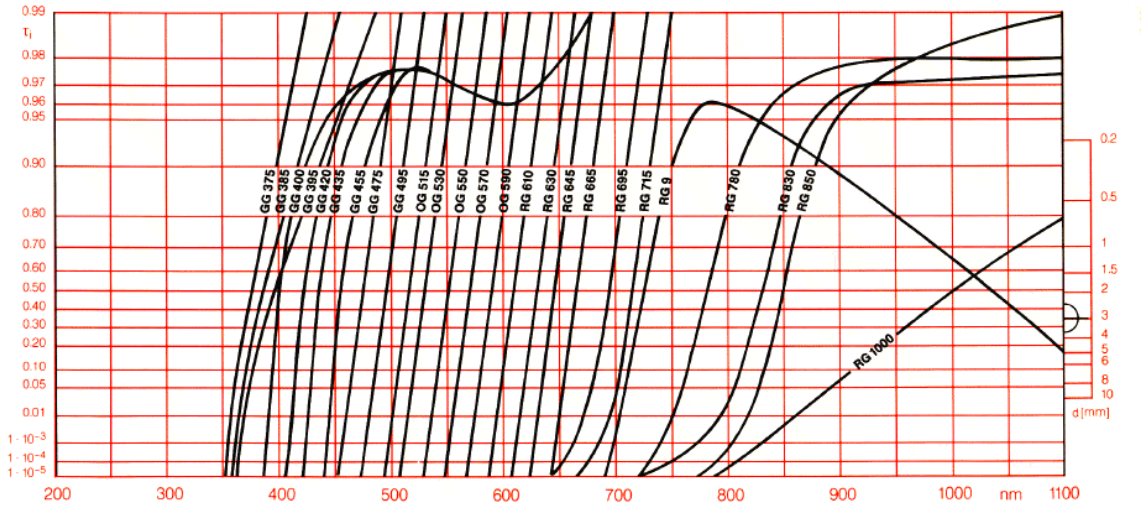

Figure 22:Rejection curves of ERFs. Different rejection curves of different ERFs.This thesis uses the RG610 filter. (Jennifer Winters, Personal communication)

The ERF stops the telescope aperture to 3.12 inches in diameter and absorbs the entire energy incident on the aperture shorter than 6000Å in wavelength.

E. Neutral density filter

This thesis therefore employs a neutral density (ND) filter to further reduce the amount of light that is incident on the chip. The ND filter employs a band selective filtering by limiting the transmittance at most wavelengths but having a high transmittance in certain wavelengths. The filter is attached to the CCD through a powered external filter wheel. The filter wheel can hold multiple filters if at any point there is a necessity to switch between filters. The transmittance of the Schott ND filter as shown in Figure 23

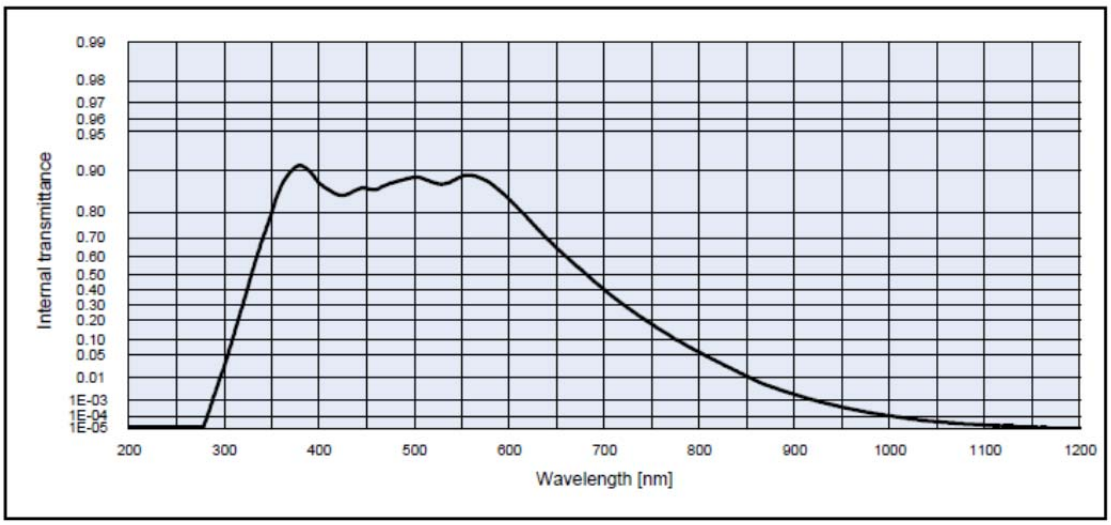

Figure 23: Transmittance of the ND filter in various wavelengths. The transmittance varies with the change in wavelength and the wavelengths which matter to this thesis have a transmittance of 0.65 Schott (2008)

As observed, the transmittance is maximum around 540 nm. The transmittance keeps dropping after this point. The approximate transmittance of the ND filter at 650 nm is around 0.65.

F. Interference eliminator

The Quantum etalon is one where the central wavelength is achieved through interference. Therefore interference fringes are a problem that occurs because of the way

in which the camera is tilted with respect to the etalon. These are the standard Newton's rings produced in high school physics experiments.

The fringes are a result of very flat optical surfaces and/or the optical components and the slight reflections among components. As the optical path length between the reflection surfaces nears a half-multiple of the wavelength of light, the light waves can add constructively or destructively in a coherent fashion, causing a peak or null in light transmission. The interference eliminator is shown in figure 23 below

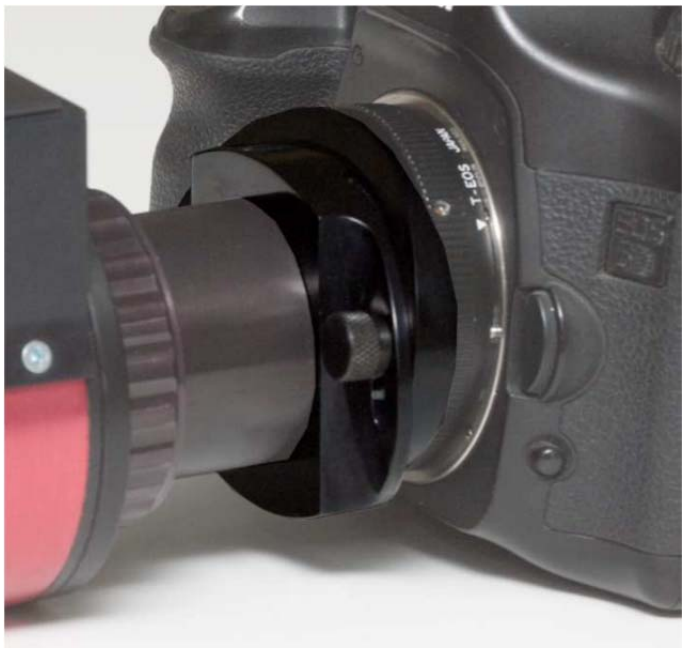

Figure 24: Interference eliminator. Moonglow Technologies, LLC. (2008)

One solution to the problem is the use of the interference eliminator in figure 24. The interference eliminator changes the alignment of light passing through these surfaces by tilting the camera so that the interference occurs at significantly higher or lower frequency, or by causing different portions of the light cone to

traverse different path lengths such that the sum total dwarfs the most pronounced peaks and nulls.

The interference eliminator works by tilting the camera, but the amount of tilt required for the camera to eliminate interference is variable and this is entirely user defined. What the author of this thesis has attempted is to reduce the interference by moving the camera using the interference eliminator. The construction of the interference eliminator has a couple of screws that can be loosened to move the camera around. The interference eliminator has a limited 5° freedom of movement provided by the screws that have brackets to move the camera.

Instrument train

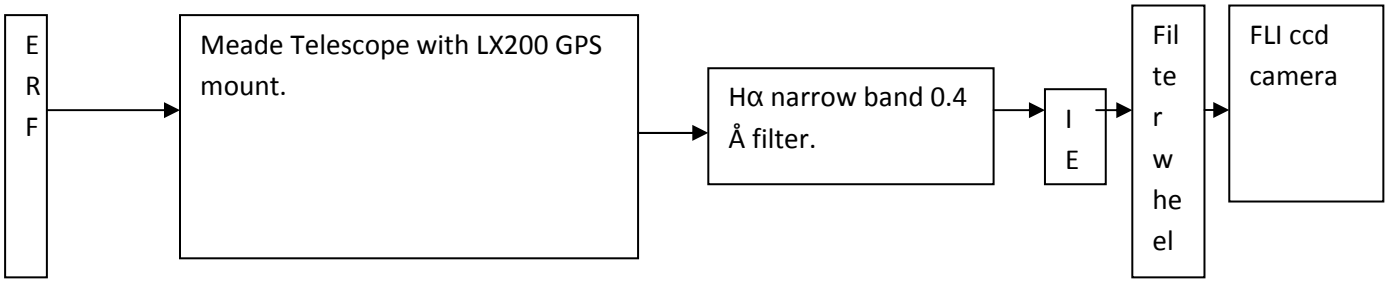

Figure 25: Instrument train. The figure depicts the entire optical system used in this thesis. The Energy rejection filter is the first element in the train on which light from the Sun is incident. The ERF then feeds the telescope which feeds the Quantum Daystar Hα 0.4 Å filter. This entire setup is connected to the FLI CCD camera by an interference eliminator mounted on the filter wheel.

The Figure 25 depicts the order of the instrumentation used in this thesis. The first element in the instrument train that faces the Sun is shown in Figure 24 from left to right. The ERF is placed in the front of the telescope over the lens of the telescope and blocks off a major portion of the light even before it enters the telescope optics. The next element is the Meade LX200GPS SCT telescope. This acts as the light gatherer and focuses the light onto the Quantum. The Quantum

filters the light and passes it on to the next optical element the Schott ND filter. The interference eliminator is another element in the optical train that is between the CCD camera and the Quantum. The IE is placed on top of the filter wheel a shown in the figure after the Quantum. The filter wheel contains the Schott ND filter which serves as a selective band reject filter. The filter wheel is mounted on the CCD camera which is the last element in the optical train.

Chapter IV: Observations

A. Introduction

Observations for this thesis involved getting at least one clear day out at the Observatory where the author was expected to image the Sun through the day. The aim of this thesis is to obtain a large number of images and evaluate the variance in seeing based on the observable features in these images. The equipment and goals of the project were defined in the spring of 2011. However, imaging has been possible on three days, 05/20/2012, 05/31/2012 and 06/02/2012. The reasons for this delay in getting images using the equipment are summarized in chronology below:

Summer 2011

The first issue identified with the equipment was in June 2011 with the temperature regulation of the Daystar. It was discovered that the Daystar filter purchased would work only within a temperature range of 65° F and 84°F. This limited temperature range was the result of the prior design and use of this filter, which included serving as a payload on at least one suborbital rocket flight (Jennifer Winters, personal communication). As this temperature range is insufficient for North Dakota weather the housing for this filter needed an upgrade. The time for this change was estimated to be approximately 3 months. Therefore no imaging was possible until Fall 2011.

Fall 2011

The test imaging was again conducted when the filter returned from Daystar on the 28th of August 2011. The test images did not show any details and the image pixel counts were extending to the non-linear range of the CCD camera. It was

unclear at that point why this was happening. One identified limitation was that the FLI CCD camera could not obtain exposures shorter than 0.06 seconds before shutter effects became apparent on the images However, the resulting test images were featureless and did not show any chromospheric details. Changing the CCD allowed lower integration times down to 0.06 seconds. But even with lower integration times there were no features and the image was still saturated. A neutral density filter (ND) was recommended by Daystar Filters with the caveat that the image resolution may degrade (Jennifer Winters, personal communication). Once an OptoSigma ND filter was used in front of the camera with a filter wheel, there was a sufficient reduction in the number of photons reaching the CCD camera, but no chromospheric features were observed. Additionally there were Newton's rings in the images. Daystar suggested using an interference eliminator to remove the rings and also that this may solve the problem of not getting any features. Additionally an interference eliminator was introduced into the growing train of equipment behind the telescope, which was now a) The Daystar filter b) The interference eliminator c) The FLI CCD filter wheel with the ND filter and d) The FLI CCD camera. Unfortunately, no features were discerned in the subsequent imaging and the last imaging attempts occurred in November 2011. The local temperatures then became too cold to use the filter and the Sun moved across the sky at altitudes too low for observing.

Daystar then requested photos of the observational setup along with the telescope. Daystar now realized that the setup was an SCT, so it needed to supply a wedge plate to compensate for the off angle exit of light from the SCT. Despite repeated clarifications that the solar imaging equipment included an SCT, Daystar somehow had managed to miss this crucial piece of information. The wedge plate for this thesis is inclined at an

angle of 1.2°. The wedge plate was then ordered at Daystar and by the time wedge plate arrived it was winter and no imaging was possible at the UND Observatory.

Spring 2012

Spring 2012 arrived early, however clear skies were significant in their absence. Even with a warm spring, the temperature needed to be above freezing (0°C) to use the Daystar filter to warm up to a uniform temperature. However a warm day never coincided with a clear day. The frustrating wait for better weather continued.

Summer 2012

The beginning of Summer 2012 brought better weather and a few initial test images with the filter did not produce any useful images despite the introduction of the new wedge plate. It was very unclear at this point which element in the instrument train was washing out the features. Daystar at this point gave an ambiguous suggestion of changing the orientation of the ERF aperture with respect to the position of the faceplate of the Daystar in a manner contrary to the instructions of the manual. This recommendation came about because the Daystar filter, which was a larger, custom built filter compared to their regular line of Quantum Hα filters, had an unknown wedge plate orientation with respect to the ERF. This position also appeared counter intuitive because the directions were to orient the ERF aperture off axis. After explicitly following the new suggestion, no change in image details was observed. The question then was, whether the ND filter was eliminating too much light in the Hα image to display chromospheric features.

To ascertain this, the author had to first ensure that the orientation of the ERF with respect to the faceplate of the Daystar was accurate. Visual inspection of the solar disk using eyepieces ascertained two things a) The description of the position of the ERF aperture was accurate in the manual and b) The orientation of the face plate did not matter with respect to the ERF aperture. The visual inspection of the solar disk also confirmed that the Daystar filter was in good working order and the problem was with the ND filter. A new Schott ND filter was ordered and the first test images with features were obtained on the 05/31/2012 with features.

Location and seeing advantages of the UND Observatory

The UND Observatory is not the most intuitive location in the world to do solar imaging; however, the location has certain advantages over regular city based backyard observing. One of the major issues with atmospheric seeing is what is called daytime seeing cells. This is primarily because of the daytime seeing being affected by the amount of heat that is reflected and absorbed off nearby surfaces. The incident light, some that is reflected, the rest being absorbed and re-radiated can cause a significant temperature increase of the local air column. The thermal cells, thus created, can affect the atmospheric seeing. Therefore constant tweaking of the focus is necessary to get a sharp, highly focused image. In places like cities this effect is pronounced because of the presence of asphalt, roofing shingles, concrete etc. However the best place to observe the Sun would be amidst grass and plains and

closer to water bodies. Laminar air flows are much better near open fields, water bodies and other smooth surfaces causing fewer convection cells.

The location of the UND Observatory 10 miles from Grand Forks makes it a reasonable location to observe the Sun because of the somewhat more favorable local environment. . The average seeing from the UND Observatory during nighttime observations is about 3", with occasional sub-2" seeing occurring (Hardersen, personal communication). Daytime seeing and seeing variations at the UND Observatory have not been previously estimated.

First trial observing run --05/20/2012

After visually ascertaining on May 18 2012 that the filter performed to satisfaction, the first sets of images were obtained on May 20 2012. The day was expected to be partially to mostly cloudy with winds and unstable seeing but improving weather towards the end of the day at the time of the partial solar eclipse. However, this day was reserved to perform two basic operations a) ensure that imaging captured all the details that the visual observing showed and b) obtain calibration flat field images.

The first set of images was obtained at 12:00 CDT. A series of 156 images each with an exposure time of 0.06 seconds were obtained over the course of the next two hours. This time was also utilized to tune the focus to achieve the "sweet spot" where the details on the disk were as crisp as possible. The Sun moved in RA from 03h:51m:24s to 03h:51m:41s and from+ 20°09'11" to +20°10'13" in Declination. The corresponding change in altitude was from +49°47'11" to 61°48'31". The first

tracking problem was noticed at this time when the mount would not track in the N-S direction when at ~61°in altitude. Not only would it not auto-track at this altitude but even manual tracking in the N-S direction was not possible. Once the Sun had reached an altitude of 57°52’52” manual aligning became possible and the image could be centered. A sequence of 50 images was shot between 14:00 hours and 16:00 hours local time (CDT). The focus was adjusted so that the dip in the histogram representing the limb was as low as it would go. This was the focus “sweet spot”.

By this time it had become clear that chromospheric features such as filaments, sunspots, and the chromospheric network were clearly visible in the images. The next task therefore was to take flat field images of blank sky and defocused Sun disk images. It was unclear at this point how flat field division was going to be achieved but it was prudent to acquire sky flats and Sun flats. The first problem with sky flats was that the image would not obtain sufficiently high counts to achieve a high signal-to-noise ratio (SNR) even with 1 minute of exposure time. This was inferred to be because of the excessive blockage of light caused by the ERF and the ND filters. The most counts received in flat field were achieved at an exposure time of 2 minutes. The count value peaked at 34,000 counts for this field. Any increase in exposure time would push the CCD into the non-linearity zone. A total of 31 sky flats were acquired.

Between 1800 hours and 1900 hours another set of 50 solar images were acquired when the Sun moved from 03h:52m:23s to 03h:52m:33s in RA and +20°12’13.3” to +20°12’43” in declination. By this time the Sun was too low in to be

observed without obstruction from the roll-off roof of IO2. Therefore 19:00 CDT is taken as the evening cut off time for imaging.

At the end of the first day of imaging, the Daystar filter, the filter wheel, the interference eliminator and the FLI CCD camera were removed and stored in the Observatory trailer before the roll on roof was drawn and images transferred to a pen drive for post processing.

Second trial observing run –05/31/2012

The second observing run occurred on 05/31/2012 as it provided the clearest weather since the previous imaging run. The weather on this day was predicted to be patchy with high wind towards the middle of the day and partly cloudy. The weather continued to be very patchy with winds and poor seeing. The clouds were present almost throughout the afternoon making imaging difficult. The author had to virtually run out of the Observatory trailer everytime the clouds cleared to get the window of opportunity to image the solar disk. The high winds of ~20 mph towards the middle of the day made the cloud cover very unpredictable. The learning from this day of imaging was that the imaging days not only need to have mostly or totally clear skies, but observers from North Dakota need to ensure they image/observe on days of little or no wind. The wind not only made the seeing variable but it also made cloud cover variable.

The first image of the day was acquired at 14:37 CDT. The imaging for this day was extremely poor primarily because of the non-uniform focus of the solar disk. The day's imaging was especially plagued by the peculiar problem of Newton's rings

towards the south/south-west region of the solar disk. This is hypothesized to be caused by the flatness of all the optical instruments involved (Jennifer Winters, Personal communication). The interference eliminator is designed to compensate for this precise problem, but in this case even with rotation of the interference eliminator the interference was not removed. Further the problem of not being able to center the disk of the Sun persisted; this problem seemed to be because of the mount but was later diagnosed to be an issue with the lack of appropriate counterweights to balance the telescope and the way that MaximDL interacts with the mount. It was impossible to center the image because of the N-S movement restriction for nearly an hour. At about 15:40 CDT the image was reasonably centered.

A total of 289 images were acquired during the day of which about 50 images did not have the solar disk at the center of the CCD. The focus on this day was difficult to determine, even when the common rule of ensuring the dip in the intensity representing the limb region of the histogram stayed as low as possible. One alternative was to magnify the prominence regions to about 400% and ensure they looked the sharpest. However the focus sweet spot did not change the sharpness of the prominences. Through the day the problems with the unfocussed edge continued to plague the imaging, but the remainder of the disk continued to churn out reasonable details. The imaging ceased at 18:48 CDT with clouds covering most of the west and the Sun being too low to actually observe over the roof of IO2.

The first burst of images was acquired between 14:37 and 14:50 CDT. At this time the sun moved from 04h:36m:25.7s in RA to 04h:36m:27.98s and +22°02’47”to +22°02’51.9” in declination. This burst was when the mount was immovable in the

N-S direction. The second burst of images was acquired between 15:50 and 18:50 CDT. This was the burst of best seeing and highest resolution. A total of 255 images were acquired in the three hours. The imaging was frequently interrupted by clouds. The major observation of this time was that the focus remained almost constant through the three hours even though the Sun moved from 04h:36m:38.1s to 04h:37m:08.58s in RA and from and 22°03'11.3"to 22°04'11.4" in declination. The corresponding change in altitude was 42°22'15.7"to 32°07'18".

Third Imaging run – 06/02/2012

The first good day of imaging for this thesis was on 06/02/2012, when all the necessary elements, the weather, the temperature, the instrument, the wind and free time came together on the same day. This was also the most eventful day where all the small miscellaneous problems were solved. The weather prediction for this day was supposed to be clear with no clouds and wind speeds of 2 mph. The temperature was supposed to be a comfortable 70°F. The atmosphere was stable at the time of arrival at the observatory. The skies were exceptionally clear with not a cloud from horizon to horizon.

The first issue in the day was that MaximDL inexplicably was unable to locate the Sun. The Sol finder on the telescope was not very rigorously aligned so MaximDL was the only software method of finding the sun. The Sun was not in the field even when the proper coordinates were entered into MaximDL. Closer inspection revealed that not only was the pointing wrong, but it was off by nearly 5°. Corrective measures

were to disconnect MaximDL and manually use the Sol finder to find the sun. However, once the sun was pointed to, tracking was as good as the Meade fork mount could give. The first image of the sun was acquired at 10:19 CDT. At this point the Sun was at an altitude of +35°01'40.1". The corresponding RA and DEC coordinates of the Sun were 04h:43m:54s and +22°16'58.5". A faint amount of fringing was observed at this time, however compared to 05/31/2012, the fringing was barely noticeable. The author had concluded after the imaging on 05/31/2012 that the Sun needs to be in the center of the field for the fringing to be negligible. The first 30 images showed very little fringing in the south-south-east of the solar disk. At the end of the first 60 images, the author decided to tweak the interference eliminator a little more aggressively. The method was to loosen the screws attaching the interference eliminator to the FLI filter wheel. Even after rotating the interference eliminator along the entire range provided did not reduce the fringing effect. The general hypothesis is that this kind of fringing can be eliminated if the range of the interference eliminator is increased. The reason for the fringing is considered to be the flatness of all the optical components involved and because of the weight present. It should also be noted that the telescope is not ideally balanced due to issues of how the telescope outer tube is designed and the lack of the necessary counter-weights and counter-weight bars. It should be noted that at this point the total counter weights attached are roughly 20 pounds which is insufficient to correctly balance the telescope. This issue later was the reason for inaccurate tracking in the middle of the day as the sun approached altitudes >60°.

The resolve was to ensure that the disk of the sun is, as far as possible, centered on the CCD. Continuous imaging was carried out for nearly 2.5 hours till about 12:30 CDT, when the first clouds began appearing the western horizon, swiftly moving towards the east. After around 12:30 CDT the mount was beginning to have some trouble consistently tracking the Sun. By 13:40 CDT the clouds had for the most part covered up half the visible sky and were slowly creeping toward the Sun. The mount also began to get to its old problem of not tracking at 61° of altitude. On inspection however, it was revealed that MaximDL was reporting the altitude as 81° when it was 61° and therefore preventing any higher northward motion of the mount. The hand-paddle also would not respond, probably because MaximDL was seizing control of the Dec motors and preventing any control signal for rotation. Therefore this had to be disconnected, the mount restarted, and the Sun manually moved to the center of the CCD. Now MaximDL was connected and tracking was enabled, this time MaximDL reported the altitude as 41° and began tracking as before!

After 13:40 CDT imaging continued in sporadic bursts because of the presence of clouds. By this time 500 images had been acquired with a total image database of 16GB. The focus across these 3.5 hours was roughly constant and needed little to no attention. The tracking however varied for every 35-40 images and the Sun needed to be recentered each time. As the Sun gained altitude this became less of an issue. The imaging after 13:40 CDT was extremely sporadic with bursts of 20 minutes at a time to ensure only a clear Sun devoid of any clouds was imaged. In the patches of clarity the seeing, stability and clarity of the image remained almost entirely unaltered. There was a continuous stream of 178 images acquired from 16:00 CDT to about 17:00

CDT. At the end of the imaging day at 17:09 CDT the total number of images was 718 and the total data collected was 22.9 GB.

The takeaway from this complete day of imaging as an exercise is the amount of data that is collectable from the UND Observatory. This gives an enormous scope to the long term science that is possible from the location.

Techniques of Data calibration

Some of the important calibration techniques that are used to process solar images include:

a) Dark noise subtraction

b) Flat fielding

These techniques are primarily important from the point of view of scientific imaging where the goal of the imaging is to ensure the scientific accuracy of the data. Dark noise subtraction is considered one of the most important calibration techniques in scientific imaging. Dark noise is the noise generated by the CCD in the absence of light. This, for silicon in a CCD, means when the thermal agitation is high enough in the absence of light, electrons get stripped off the valence band and collect in the potential well of the pixel. This manifests itself as activated pixels where there should be no activation. The dark current is usually specified by the manufacturer of the CCD to give the user and idea of how much dark current he can expect. The dark current of the FLI CCD is <0.07 electrons/pixel/second at a -35° C CCD temperature.

Reduction in dark current is accomplished in two ways. One way is to cool the CCD to a low enough temperature that there is little or no dark current. A typical

temperature plot of the dark current is shown in Figure 26:

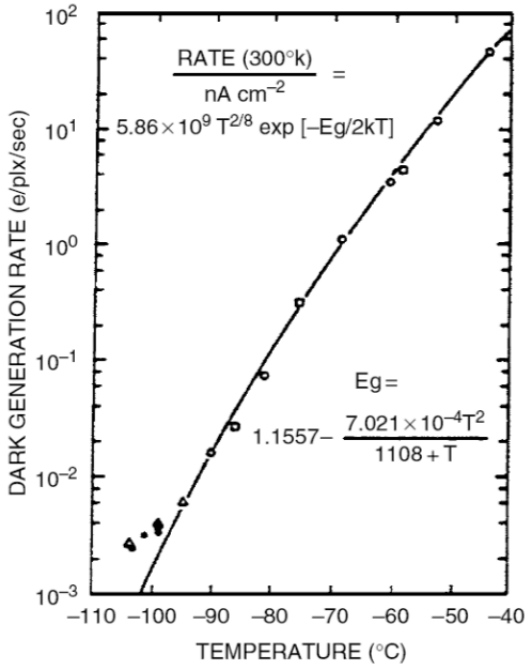

Figure 26 : Temperature dependence of the CCD dark current. With lower CCD temperatures the amount of dark current reduces. The dark current can reduce to such low values that it is negligible (Source : Howell(2006))

The idea therefore is to cool the CCD down to as low temperatures as possible, lowering the dark current to very low values. This dark current is then eliminated using a procedure known as dark current subtraction. In dark current subtraction, a certain number of images (recommended about 10-20) are obtained at exposures comparable to the exposure of the image. These are then averaged to create a dark frame and then subtracted from the original image, yielding a dark subtracted image.

Flat fielding is the technique of obtaining calibration images to flatten the relative response of each pixel to the incoming radiation. Ideally a flat field image should have uniform illumination of each pixel by a light source of identical spectral response to that of the object frames. The flat field images thus obtained are averaged and divided from the original to yield a flat divided version of the original image. In this case, the flat field image was a two minute exposure of a section of the blank sky. The standard procedure is

to have about 10-20 flat field images which are then averaged to produce a master flat field frame. In this case, there were 30 flat field images which were averaged using MaximDL to create a master flat field frame.

This thesis has had specific problems with flat fielding. The flat field images were divided from the original raw image using MaximDL. This division removed some of the image artifacts such as lines in the CCD but was unable to get rid of real image artifacts like the dust on the image. One of the issues it seemed was the flat field image was not illuminated enough, but even with that it is unclear why the flat field division did not get rid of artifacts present in the original flat field image that should have naturally divided out.

One solution was to create flat fields using the solar surface as the flat field divisor. However, the suggestion to do this involved imaging the sun across quadrants. This was attempted, but was very difficult to consistently do as the movements have to be very precise and it is difficult to measure on the field whether the mount moved as precisely as it should have moved. The time allotted for this thesis did not allow enough experimentation to adapt the technique to the UND Observatory equipment. This is a potential issue that should be solved probably in a future student project.

Focus adjustment and variance

Focus forms an important function in this thesis of ensuring that the image remains the sharp and the features are in the best contrast. Figure 26 depicts how the focus varies over different images on different days. The focus is altered by twisting the focus knob on the telescope which changes the position of the primary mirror slightly to produce a focused image on the CCD.

In order to determine the point of accurate focus, this thesis looks at the contrast between limb and the background and the lowest value of this contrast is the best focus.

The Figure 27 determines the lowest RMS contrast values for different images on different days. This is obtained by taking the counts at the point of lowest contrast in images on all 3 days with different images. The highest counts here correspond to the defocused images with low contrast. The Figure 27 depicts the improving contrast with change in focus. The poorer focus corresponds to higher RMS values and lower values correspond to better focus.

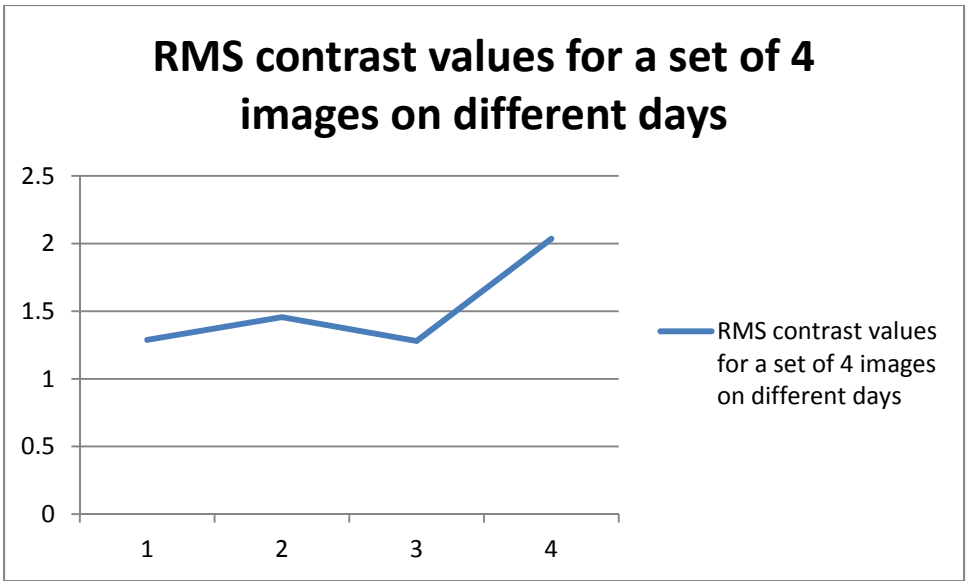

Figure 27: The y-axis gives the value of the RMS contrast for a set of 4 different images on different days, the x-axis is the images over which the focus varies.

Throughput of the system:

The throughput of the system is a measure of the amount of data that this thesis has to work with, with respect to the total available data. To calculate this it is necessary to understand the elements which make up the optical path. Firstly the light is filtered by the ERF to wavelengths higher than 600 nm. This reduces a significant amount of light from entering the system. The next light blocking element is the Quantum which has a narrow band transmittance of 0.4Å. Finally the last element is the Schott ND filter which blocks light between 600 and 800nm in this setup.

Calculation: The optical window of the earth's atmosphere lets in light roughly between 550 nm to 750 nm. The ERF blocks all light below 600nm. Therefore the ERF lets through only 75% of the light. The Quantum operates between 656.24nm and 656.32 nm. This is 0.08nm out of 150nm, the percentage works out to 5.33×10^{-6} % of the light incident on the optics. The Schott filter has a transmittance of 0.65 at 630nm. This translates to roughly 3.2×10^{-6} % of the light being received by the CCD camera. In ratio of the total light received by the earth only 3.2×10^{-4} is actually recorded in the CCD.

Chapter V: Results and analysis

Software and techniques

This thesis is an instrumental thesis; the results and analysis will primarily constitute describing the variance in atmospheric seeing and the image processing algorithms implemented. Image processing for this thesis was primarily done with three different software: a) MaximDL V5 b) SAOImage DS9 c) Interactive Data Language (IDL).

MaximDL Pro

MaximDL is a camera and telescope operating software that is designed for a Windows system. It operates scientific-grade CCD cameras, DSLR cameras, low-cost CCD imagers, and webcams and other video sources. It also controls filter wheels, focusers, autoguiders, telescopes, focal plane rotators, and observatory domes. A wide variety of hardware is supported through both ASCOM drivers and proprietary and third-party plug-in drivers.

This thesis used MaximDL Pro to perform two activities a) to control the telescope mount and b) to control the camera and the filter wheel. The telescope control is achieved using the Observatory Control Window. The observatory control window has the ability to control the dome, the telescope and find objects using the object finder. This thesis uses this function to slew to the Sun by manually entering the values of the RA and Declination of the Sun using the SkyX software.

The Camera Control tab is used to control the camera. The camera is externally powered but, the control for the camera originates at the computer in IO2, and with MaximDL. The camera control can achieve integration times as low as 0.001 seconds. Observations are limited by camera shutter effects and the integration time can be as low as 0.06 seconds.

The other functions of MaximDL used for observations and image analysis include: a) histogram stretching b) basic image processing which includes unsharp masking and layering, and c) flat field image acquisition and creating the master flat. The image processing function is perhaps the most basic function used to evaluate the quality of images. Higher advanced image processing in this thesis is achieved using the Interactive Data Language (IDL). Other simpler functions such as stacking, aligning etc are possible within the MaximDL framework. This thesis has a special requirement from MaximDL in that instead of low light conditions that the software is tailored to, it is exposed to a very bright condition.

SAOImage DS9

SAOImage DS9(DS9) is an image analysis software that has been primarily used in this thesis as a tool to evaluate image quality by looking for the size of specific features using the selection tool. DS9 is an open source software with most of the software packages freely distributed by the Smithsonian Astrophysical Observatory, Cambridge , MA. DS9 versions are available for Windows, Mac, and Linux. DS9 can also be used to layer frames, stack images and simple image processing. This thesis uses

the selection tool to select the feature whose size is being evaluated pre and post processing.

Interactive data language (IDL)

The interactive data language (IDL) is an array oriented data analysis and visualization environment for data manipulation.IDL is used for multiple things including image manipulation and analysis. This thesis uses the Macintosh version of the IDL development environment (IDLDE). IDL is primarily an array manipulating code base and most of the commands are executed from the command line. IDL is primarily used to supplement the usage of some basic algorithms implemented in MaximDL such as wavelets and highpass filter implementation. Also IDL offers some level of flexibility in terms of the size of kernels etc.

Seeing and image results

The quality of images acquired has been very variable. One of the interesting observations of the author has been that the variability of seeing does not just happen over a day, but the seeing varies from image to image. The seeing was evaluated by looking at a)The clarity of specific features like sunspots, prominences and filaments b) size of the features in terms of radial distance from the center and c) the contrast of the feature which enhances the feature characteristics like the boundary and distinction between constituent elements like the umbra and penumbra. The following image examples are from the imaging run on 06/02/2012.

An example of very poor atmospheric seeing is presented here in Figure 28

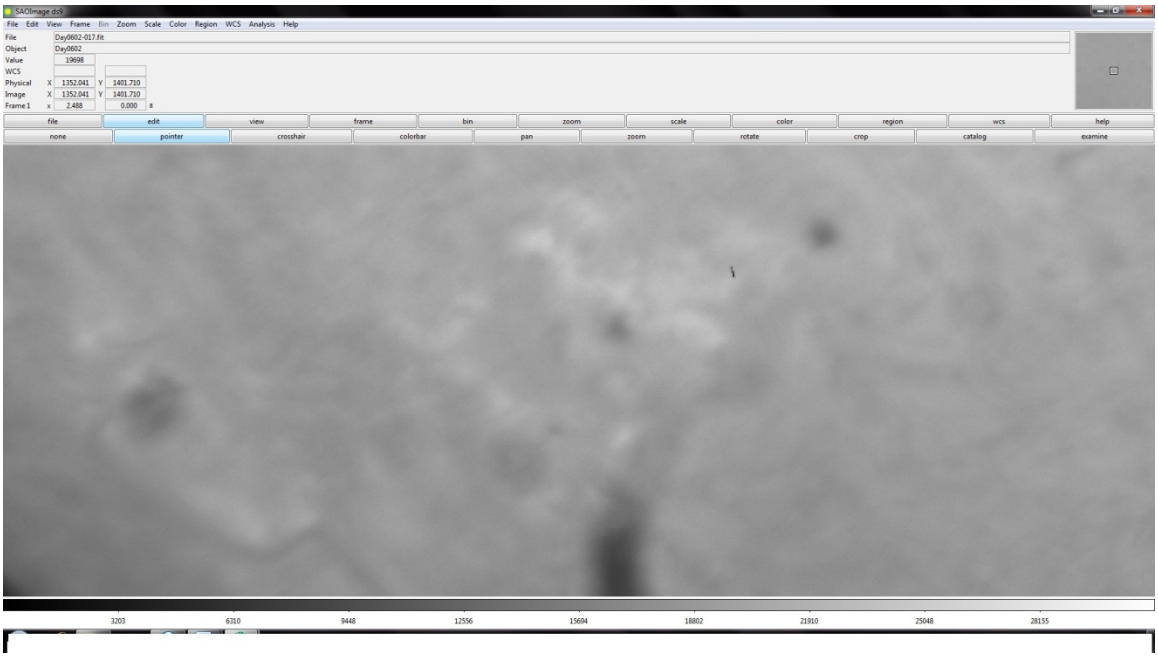

Figure 28: Example 1 of poor seeing. The image represents imaging through bad seeing. The image depicts a sunspot and the surrounding active regions, but there is no clear demarcation of the extent of the active region(AR 11493) and the filament in the lower left of the image is barely visible.

Figure 28 shows an active region with a filament at the bottom of the image. The hallmark of the bad seeing has been the lack of demarcation of the active region extent. The sunspot is also poorly resolved and lacks any kind of morphological detail. The contrast is poor and the filament which is quite large is not distinguishable from the background material. Also the sharpness and accuracy of the active region is very poor. The surrounding material in the active region is also not resolved and does not seem to be affected by the presence of the active region.

Conversely Figure 29 represents an image where the seeing was much better and the resolution seems to have automatically improved.

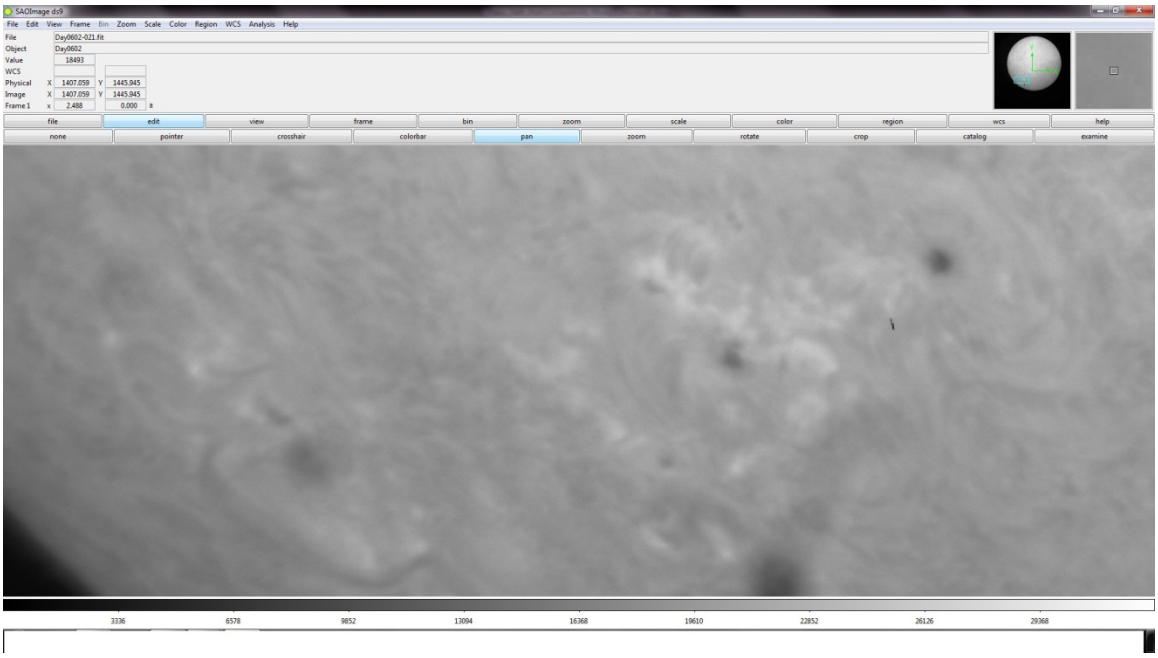

Figure 29: This is an example of improved seeing over time. The features in this are accentuated and stand out much more clearly than in Figure 28.

Figure 29 shows the same AR11493 as in Figure 28 and the improvement in seeing is characterized with the improvement in demarcation of the extent of the active region. The sunspot also shows very good morphology. The distinction between the umbra and penumbra is palpable. While measuring the size of the umbra in this image there was no ambiguity in where the umbra was, while this was difficult to characterize in figure 28. The filament on the lower left corner is highlighted implying an improvement in contrast. The material around the AR also show clear flow patterns towards the AR. The region where the effect of the AR is absent shows patterns of material characteristic of the chromospheric network. The brighter active regions have better contrast to the non-active chromosphere.

On limb prominences do not reveal this distinction as much but there is some improvement in the resolution of prominence structures with seeing. Figure 30 shows how prominences appear in an image where poor seeing is observed.

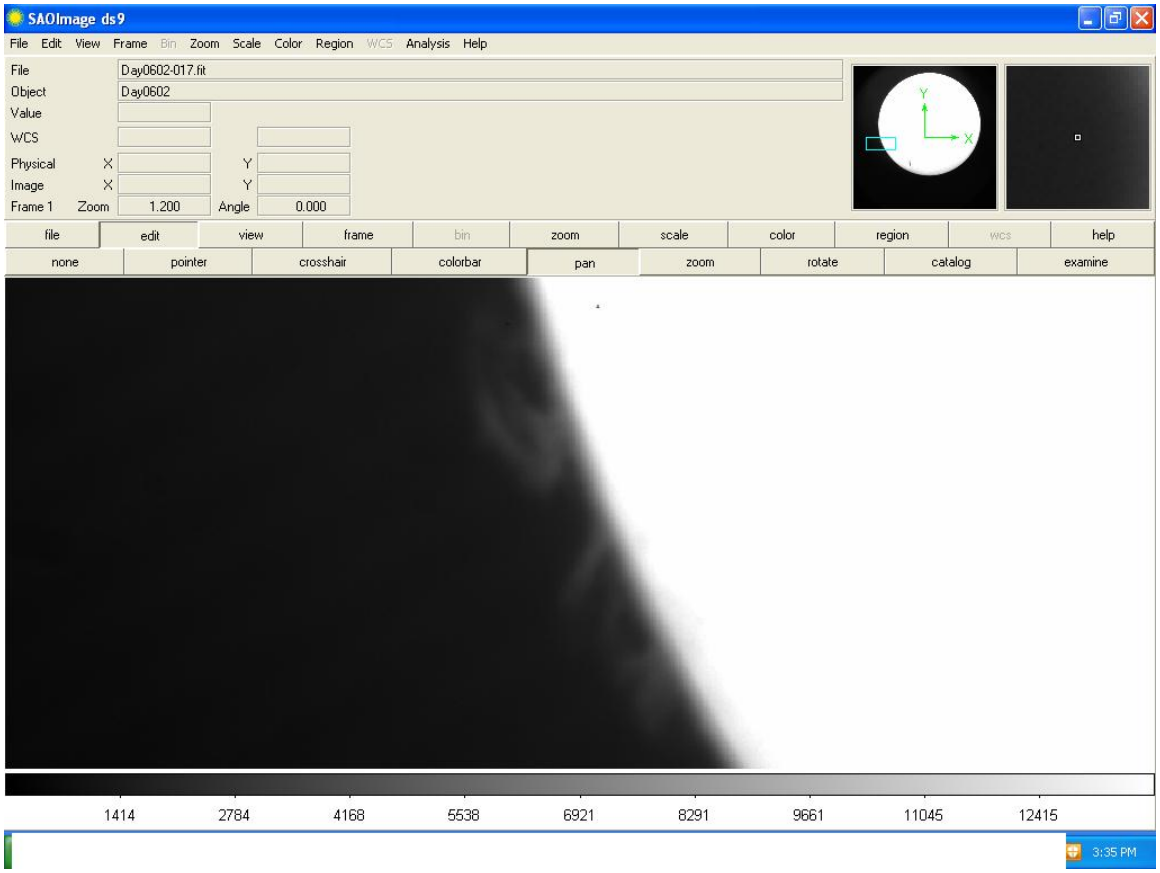

Figure 30: Example 2 of poor seeing. This shows the resolution of prominences by varying the screen stretch to reveal the limb feature. The effect of poor seeing is predominant in how poorly the structure within the prominence is revealed.

Figure 30 shows prominences on the limb. The prominences have specific structure, but it is not possible to tell what kind of prominences these are because of the poor resolution of their structure. Their physical connection with the chromosphere also is poorly defined. This image shows the prominences as just jets of material emitted from the chromospheres with no specific morphological features. Figure 31 on the other hand shows that these prominences have a defined structure and the topmost prominence is a

loop prominence because it connects back to the chromosphere. Though there has been no other means of asserting this is a loop prominence, circumstantial evidence points to it being a loop prominence.

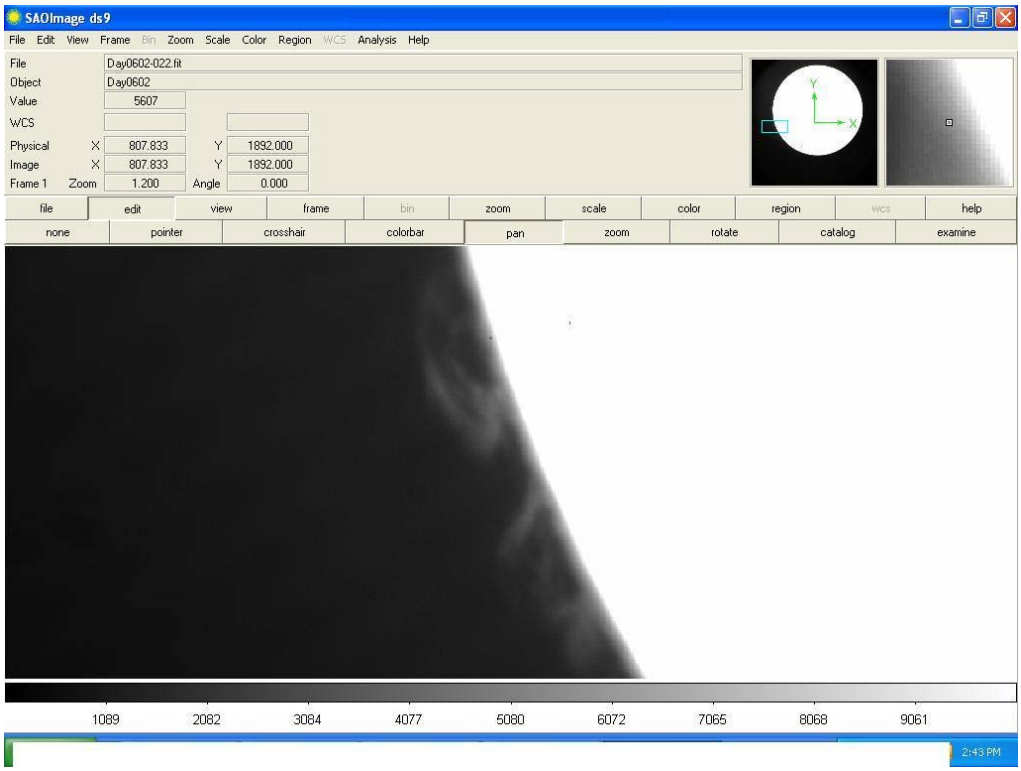

Figure 31: Example 2 of good seeing. This is an example of prominences with clear structure and morphology owing to improved seeing over Figure 30. This image shows improved structure in all the prominences observed in Figure 30.

Figure 31 shows the topmost prominence having a loop like structure and connecting back to the chromosphere with a thin band of material. The prominences also show some form material exchange in the bottom two prominence structures. Interestingly this improved seeing also shows material on the base of the prominence structure.

The master flat for these imaging runs is displayed in Figure 32.

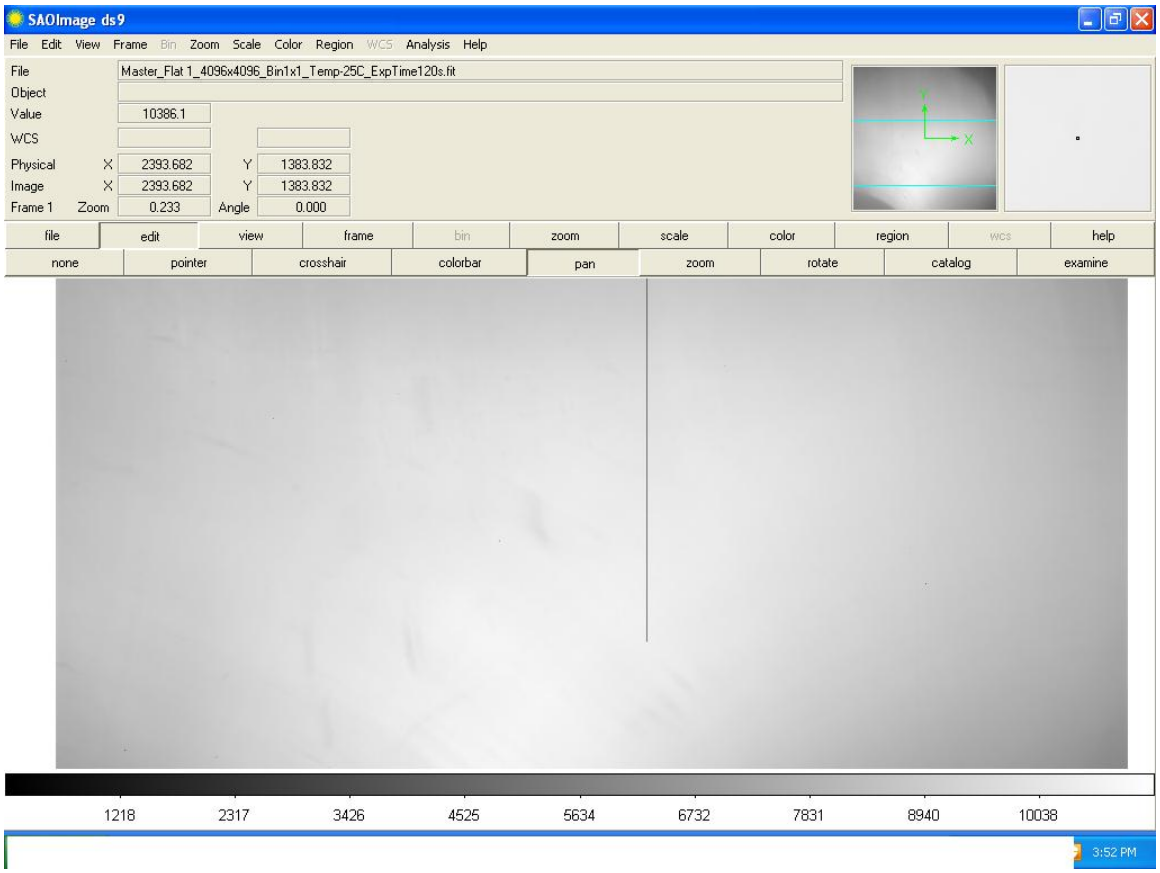

Figure 31: Master flat for the images used in this thesis. It shows the image artifacts like the line in the center and the dust in the equipment.

The master flat shown in Figure 31 was divided out of the images to give flat divided images. It was however not very effective because of low amount of illumination of the dust as seen. This dust continues to be a presence in the images and has been one of the issues with the calibration. The method of removal of dust involves imaging of the solar disk which time did not permit. This can be a probable future student venture to remove the dust using a standard method from the data.

The results from the images here have been expected. The seeing variations are more than anticipated by the author but the variations themselves were not unexpected. As a pre-cursor to estimating daytime seeing from the UND Observatory, this thesis has

attempted to evaluate the change in the seeing by looking at the changing size of the umbra in two different sunspots from 05/20/2012 and 06/02/2012. The plots of the change of the umbral radius are shown in Figures 33 and 34. The key take away from these plots is the trend of variance of seeing which would be a function of the changing size of the umbra. For stable seeing the change in size should be very little but the plots here correspond to a high variance. The question is whether image processing techniques will change/improve the seeing in these kinds of atmospheric variations.

Procedure:

DS9 is used for measuring the radius of the sunspot. The image is first opened using DS9 after calibration. The appropriate sunspot is panned to using the pan tool and a zoom of more than 400% is implemented. Then using the pointer tab, a circle is drawn around the umbra of the sunspot as shown in Figure 33

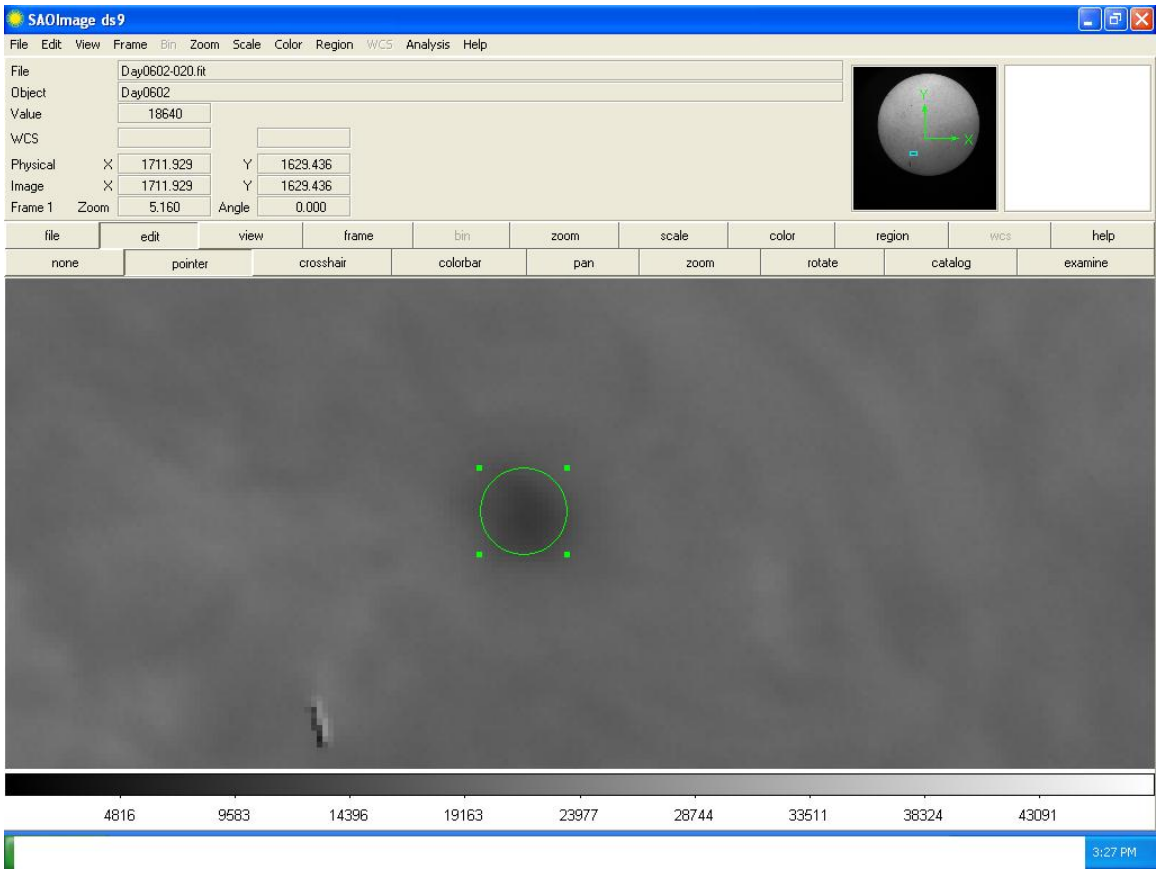

Figure 33: Measuring the radius. The sunspot is selected using the pointer tab and a circle is drawn around the sunspot umbra.

The circle now represents the size of the sunspot. Double clicking this sunspot now gives the radius of the circle in a new tab.

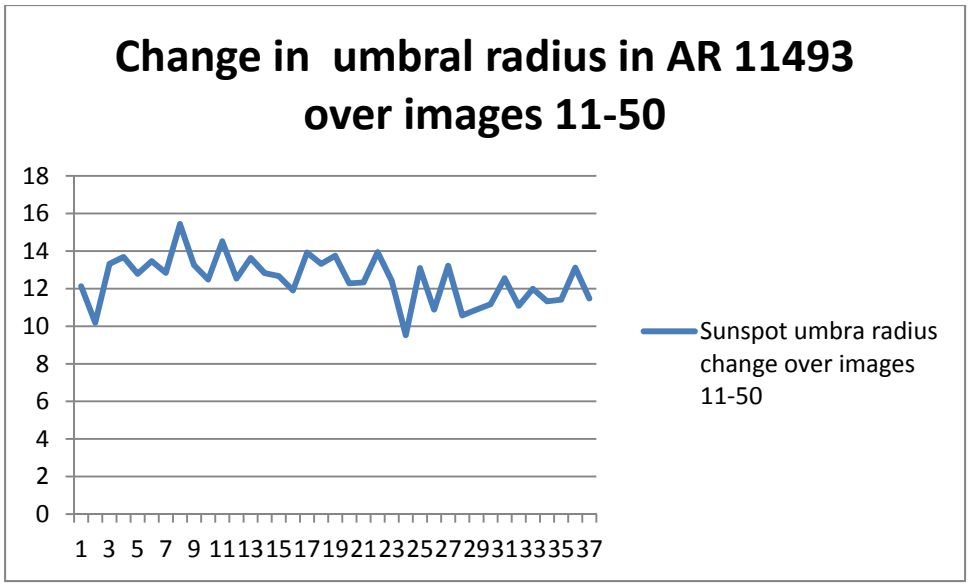

Figure 34: Change in the radius of the umbra in pixels on 06/02/2012. The change in radius in pixels is plotted on the y-axis versus the image number on the x-axis. Images are sequentially obtained. This represents the change in seeing over a period of 37 subsequent images.

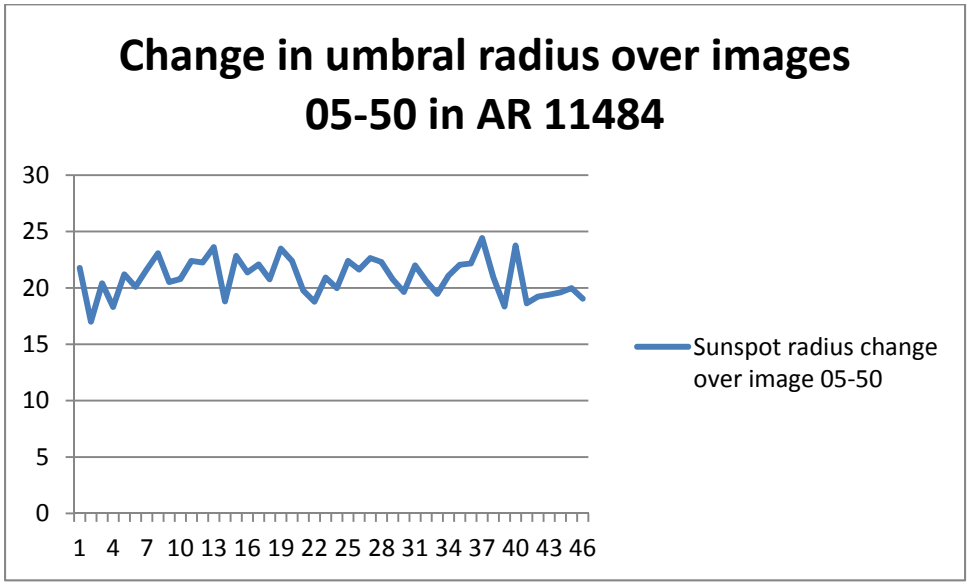

Figure 35: Change in the radius of the umbra on 05/20/2012. The change in radius is plotted on the y-axis versus the image number on the x-axis. Images are sequentially obtained. This represents the change in seeing over a period of 45 subsequent images.

RMS contrast values for the data

RMS contrast is used in this thesis as another proxy for measuring atmospheric seeing. The size of sunspot is measured and its change is plotted in Figures 34 and 35. The RMS contrast for the same sizes is measured by subtracting the average and dividing it by standard deviation.

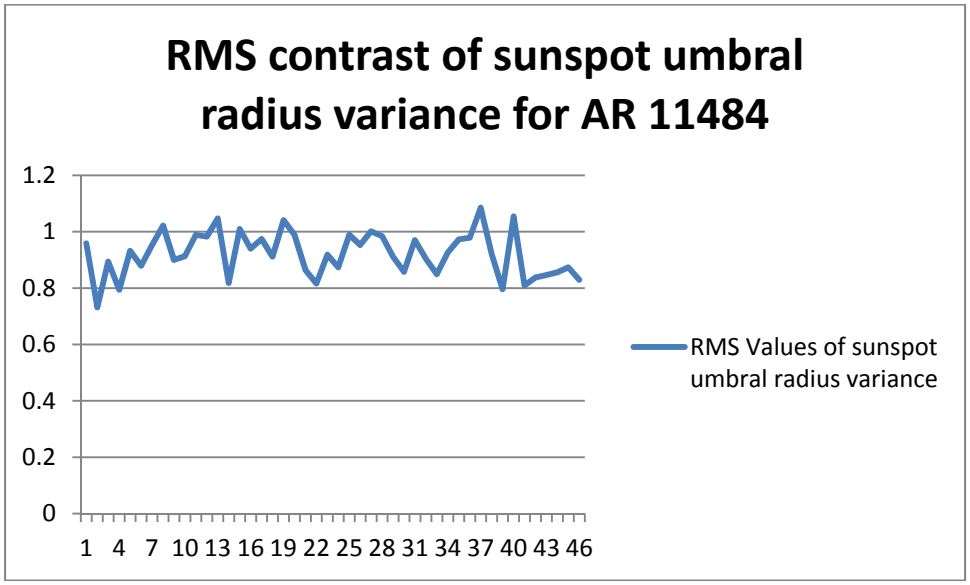

Figure 36:RMS contrast for values in images on 05/20/2012. RMS contrast values on RMS contrast values in the y-axis and the image number in the x-axis represent a proxy for the seeing variance.

The RMS contrast values of the umbral size of the sunspot in AR 11493 are plotted below. This is another proxy for the variance in the seeing over a number of images.

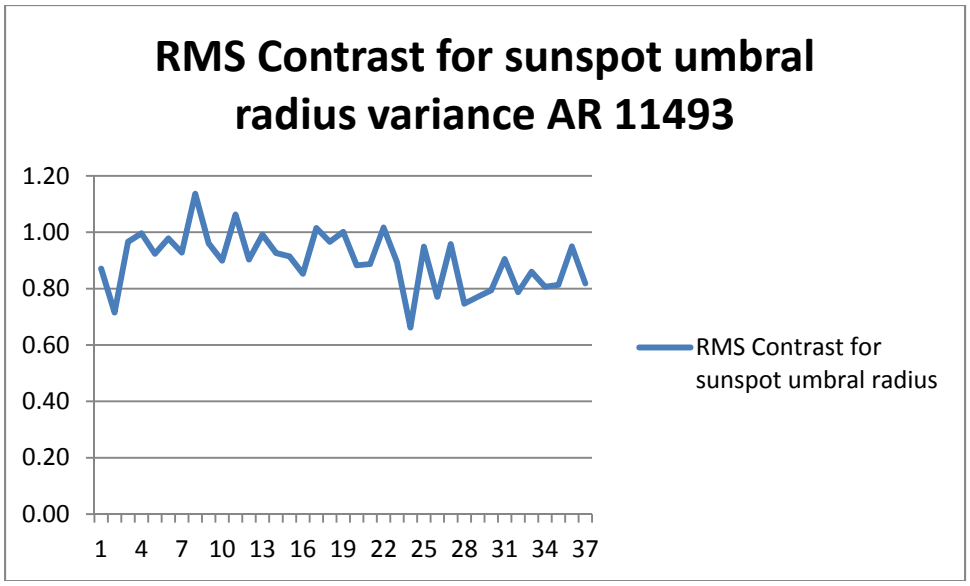

Figure 37: RMS contrast for values in images on 06/02/2012. RMS contrast values in the y-axis and the image number in the x-axis represent a proxy for the seeing variance.

The RMS contrast is representative of the change in contrast with seeing. This quantity measures the standard deviation of the contrast of pixel intensities. The trend is quite similar to the trend with change in sunspot sizes.

Image processing:

In order to determine whether image processing algorithms produce any significant improvement in contrast, different kinds of processing algorithms have been implemented. Each algorithm uses the different software programs for specific purposes. IDL has been used primarily where processing techniques using MaximDL have not been flexible enough or have been inaccurate. This thesis does not offer any kind of final solution to the problem of processing images. The goal is to attempt different processing methods and estimate how useful they are in improving the overall image quality. These image processing techniques described here are by no means a complete and comprehensive list but are representative of the kind of processing that could be done.

The algorithms selected, are intended to enhance the features on the disk of the sun. Therefore, primarily high pass filters or sharpening algorithms have been applied. The idea is that the contrast of the image is increased with the use of either high pass or sharpening filters. This enables the observer to more clearly distinguish the boundaries of chromospheric features such as filaments and the chromospheric network. The key is to detect accurately the edges of the features and distinguish them from the overall surface of the Sun. In selecting algorithms for this thesis, care has been taken to ensure that there is no selective application of the algorithms and the analysis is conducted on the entire disk of the Sun. This is so that the processing is carried out on the whole disk of the sun and not just a portion of it and the quality of this algorithm is to be evaluated only if the processing enhances the full disk image of the Sun. The IDL algorithms applied are listed below

a) Adaptive histogram equalization (AHE): The seminal work on this technique has been done by Pfizer et al(1986). AHE is designed to enhance the local contrast of an image by altering the pixel values based on surrounding pixel values. The difference between the standard histogram equalization and AHE is that AHE improves the contrast by transforming each pixel with a transformation function derived from a neighborhood region. In its simplest form, each pixel is transformed based on the histogram of a square surrounding the pixel. This thesis tried using this technique without any success. One of the problems of this technique was the absence of any kind of contrast in the image post processing. AHE was implemented by this thesis using IDL. The function call for this procedure is ADAPT_HIST_EQUAL**.**

The syntax of this function is Result = ADAPT_HIST_EQUAL (Image [, CLIP=value] [, FCN=vector] [, NREGIONS=nregions] [, TOP=value]). Here the Result is where the image array after AHE processing is stored and Image is the image that is to be processed. The keywords that can be varied are explained here : CLIP-- Set this keyword to a nonzero value to clip the histogram by limiting its slope to the given CLIP value, thereby limiting contrast. For example, if CLIP is set to 3, the slope of the histogram is limited to 3. By default, the slope and/or contrast are not limited. Noise over-enhancement in nearly homogeneous regions is reduced by setting this parameter to values larger than 1.0. FCN--Set this keyword to the desired cumulative probability distribution function in the form of a 256 element vector. If omitted, a linear ramp is used, which yields equal probability bins results. This function is later normalized, so magnitude is inconsequential, though should increase monotonically. NREGIONS-- Set this keyword to the size of the overlapped tiles, as a fraction of the largest dimensions of the image size. The default is 12, which makes each tile 1/12 the size of the largest image dimension. TOP-- Set this keyword to the maximum value of the scaled output array. The default is 255.(Source: Landsman, W. (2010)) This method however did not yield acceptable results and was rejected.

b) Robert's edge enhancement algorithm: The Robert's edge enhancement algorithm is a contrast enhancement algorithm. Like any edge enhancement algorithm it enhances the local discontinuities at the boundaries of different objects (edges) in the image. This algorithm has a different kind of kernel

compared to other algorithms. This kernel focuses on the diagonal pixel differentials, which emphasizes corners more clearly but can blur together small horizontal or vertical features. The operation is akin to using convolution masks with kernels

$$\begin{bmatrix} 0 & -1 \\ 1 & 0 \end{bmatrix} \text{and} \begin{bmatrix} 1 & 0 \\ 0 & -1 \end{bmatrix}$$

This was also implemented using IDL and the syntax is

Result=Roberts(image).

The problem with this algorithm was that even though it brought out details, it wiped out most of the other features of the sun like gradation of color across the surface and opacity making the sun almost a transparent disc. (Source: Landsman, W. (2010))

c) Sobel transform: The sobel transform is another edge enhancement algorithm that works like the Roberts edge enhancement transform. Here the masks used are

$$\text{X mask} = \begin{bmatrix} -1 & 0 & 1 \\ -2 & 0 & 2 \\ -1 & 0 & 1 \end{bmatrix} \qquad \text{Y mask} = \begin{bmatrix} 1 & 2 & 1 \\ 0 & 0 & 0 \\ -1 & -2 & -1 \end{bmatrix}$$

This transform is implemented in IDL for this thesis and the syntax for this is

Result=sobel(image)

Then results from the sobel transform were much better than those obtained using the Robert's edge enhancement algorithm in terms of enhancement of features. However the same problem was observed with the Robert's algorithm in that it eliminated all other surface details like opacity and presented a transparent disk with the features highlighted as shown in figure 38

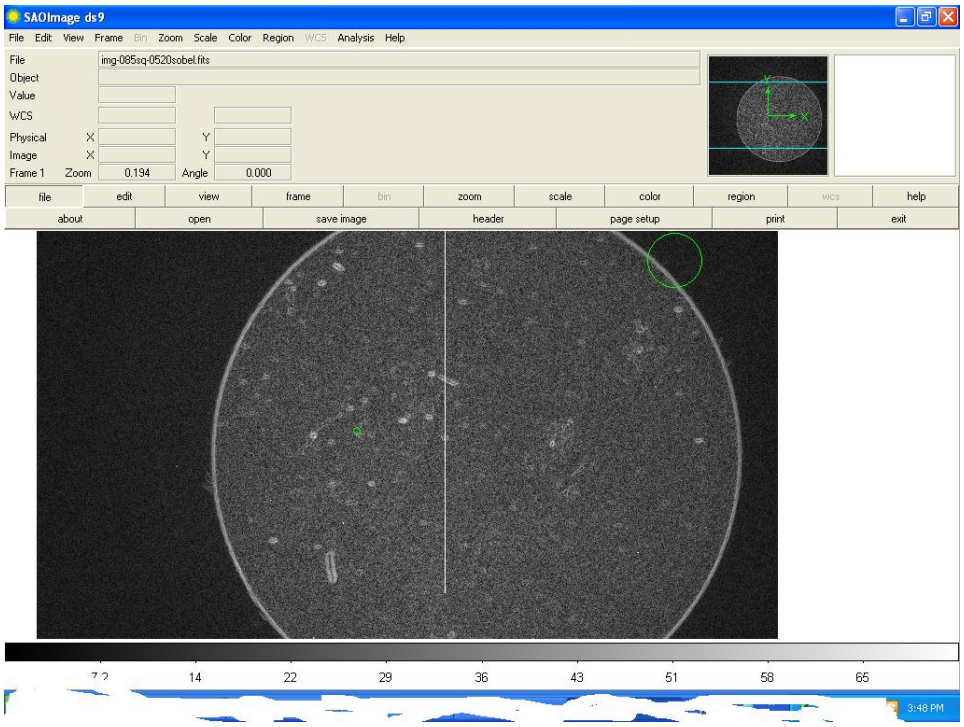

Figure 38: Result from Sobel transform. This figure depicts the result of image transformation using the Sobel transform to enhance the edges in the image. The transform highlights specific details in the active region on the right of the image and prominences at the limb. However it does not represent the opacity of the disk or the chromosphere.

d) Unsharp mask: An unsharp mask is a two step process designed to improve image contrast. The procedure involves a) Creating a smoothed version of the original using a Gaussian blur b) compare the smoothed version to the original and if the difference is less than a specified threshold then the images are subtracted. This technique was also attempted using IDL. The syntax for

unsharp mask in IDL is Result = UNSHARP_MASK(Image [, AMOUNT=value] [, RADIUS=value] [, THRESHOLD=value] [, TRUE={1|2|3}]) where the result is the unsharp mask of the original image stored in the array Image. The other key words here : AMOUNT--Set this keyword to a floating-point value giving the amount (or strength) of filtering to be applied. The default is AMOUNT=1.0, which implies that 100% of the filter difference will be applied to the *Image*. AMOUNT may be negative, which will have the effect of blurring the image instead of sharpening. RADIUS-- Set this keyword to a floating-point value giving the radius in pixels of the Gaussian smoothing filter. The default is RADIUS=3. The Gaussian filter is designed to fall to 1/e (~0.367) at a distance of RADIUS/sqrt(2). The total width of the Gaussian filter is given by ceil(2 * RADIUS)/2 * 2 + 1 (if RADIUS is an integer then this is just 2 * RADIUS + 1). THRESHOLD-- Set this keyword to a non-negative integer (or a floating-point if *Image* is floating point) giving the clipping threshold. For each element, if the absolute value of the difference between the original image and the low-pass filtered array is greater than or equal to THRESHOLD then the filter is applied to that point. The default is THRESHOLD=0, which implies that every point will be filtered. TRUE--If *Image* is a three-dimensional array (a multichannel image), set this keyword to 1, 2, or 3 to indicate which dimension represents the channels. The default is 1, for pixel interleaving, (3, *m*, *n*). A value of 2 indicates line interleaving (*m*, 3, *n*), and 3 indicates band interleaving, (*m*, *n*, 3).

The image processing in this case however produced an overall lowering of the intensity of the image. This was not acceptable as this was not representative of the original data that was recorded. Figure 38 is an example of the lowering of intensity of the pixels. (Source: Landsman, W. (2010))

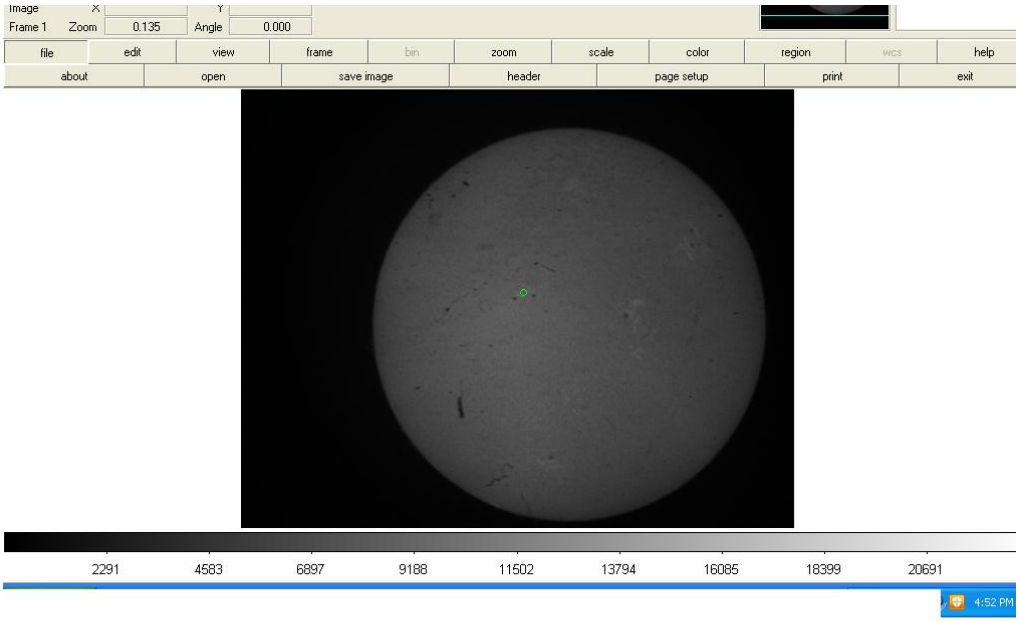

Figure 39: Sobel transform. This is an example of the unsharp mask technique which reduced the overall intensity of the image. The maximum counts went down from being close to 25,000 to about 9000 counts. As this does not represent adequately the solar surface or its intensity this technique was rejected.

e) <u>High pass filter using convolution kernels</u>: This was the best method that worked for sharpening an image. A standard high pass kernel looks something like $\begin{bmatrix} -1/9 & -1/9 & -1/9 \\ -1/9 & 8/9 & -1/9 \\ -1/9 & -1/9 & -1/9 \end{bmatrix}$ (Source: Landsman, W. (2010)). The standard method of creating a high pass filter

using kernels is to convolve the original image with the kernel. The kernel's operation is defined by the value of the central element in the matrix also called the central factor of the kernel. Trial and error prescribed a value of 30 in the numerator of the matrix displayed here. This produced the highest value for the radius of the active region spot. Any value above 30 did not produce any significant difference. Figure 39 displays both the images before and after processing.

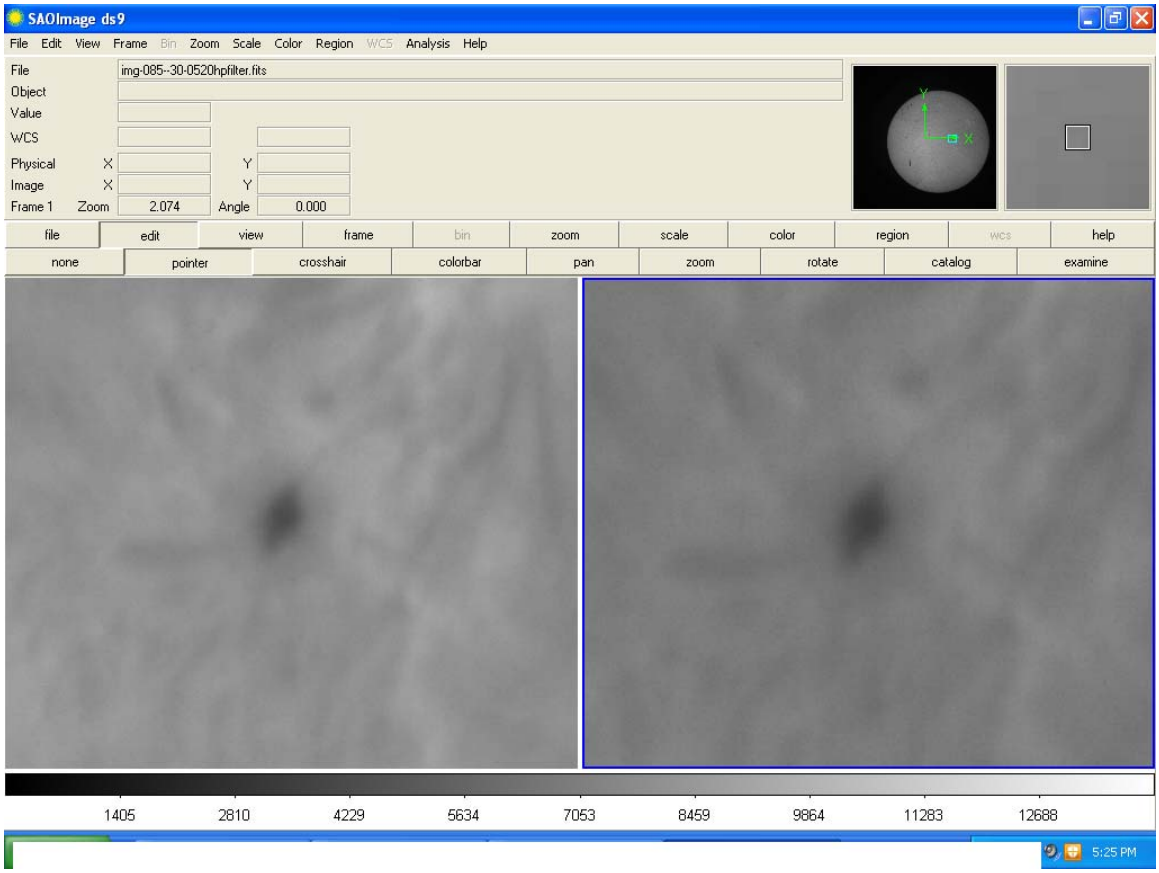

Figure 40: Processing with IDL high pass filter. The image on the left is the post-processing result of the same area in AR 11484. It is clear that after processing the contrast between the umbra and the penumbra is greater and the spot is more defined. The radius of the spot on the left is 23.4 pixels while the one on the right is 26.86 pixels. This change corresponds to a difference of 2.5 arcseconds.

This method has been implemented using IDL. This method uses high pass filter kernels convolved with the original image to get the appropriate enhancement. The evaluation of this method is exactly the same as the Wavelet edge enhancement. The size of the spot is evaluated before and after processing using DS9. This method consists of a 3x3 matrix as the kernel. This kernel is generated using IDL methods. The matrix used in this technique is such that the sum of all the elements of the matrix is 1. The standard high pass filter matrix consists of negative elements in all the rows and columns except the central element. However this is just a standard matrix and this is not a rule. The matrix in the method used in this thesis has a central element value of 30, and therefore the sum of the elements does not add up to 1. The intention of course here is to choose the best kernel that will give better results with the images. It has been observed that using 30 as the central element gives the best results. The mathematical justifications for this have not been probed into and are not the object of this thesis.

Procedure: The procedure is roughly the same as the Wavelet Edge enhancement, except that the primary processing is achieved using IDL code on a Macintosh. The IDL used in this thesis is IDLDE 8.1. The interface is primarily a command line interface. Before the start IDL needs to be able to read FITS files, this thesis uses the fitsread.pro method to read FITS files. This method needs a lot of pre-requisite functions, so a considerable time has been spend on building the dependencies for FITS operations. Once the dependencies have been built, IDL should be able to read FITS files with no

further issues. Image display on IDL is not very well implemented, it is hard to scale images and view them comfortably, and therefore it is recommended to use other programs to view the results. This thesis uses DS9 to view the results and evaluate them. Once the image has been read into an array, the array is operated on with a kernel generated by the following piece of code:

```
kernelSize = [3, 3]
kernel = REPLICATE(-1., kernelSize[0], kernelSize[1])
kernel[1, 1] = 30
```

The kernel then is convolved with the image using

```
    filteredImage = CONVOL(FLOAT(Image), kernel, $
/CENTER, /EDGE_TRUNCATE)
```

This stores the result of the convolution in the array filteredImage. This is then saved onto disk using the writefits.pro routine. The writefits.pro also requires a large amount of dependency building and a considerable amount of time was spent building these dependencies. It is highly recommended that when doing basic fits operations, to look at what dependencies need to be built before embarking on the actual processing.

<u>High pass filter using Fast Fourier Transforms(FFTs):</u>

High pass filters were attempted using FFTs in MaximDL. FFTs are efficient methods of obtaining the Fourier responses of images. Fourier transforms applied to images result in the frequency responses of the individual pixels in the image. However, just transforming an image is not the objective, using the

FFT to retain just high frequency components of the image should lead to sharpening the image and enhancing the edges of the image. MaximDL applies the FFT and transforms the result back and mixes the result with the original image. The "hardness" of the filter measures the radius within which the low frequencies are suppressed. This is defined by the cutoff parameter of the FFT. The FFT filters in MaximDL have a Butterworth characteristic.

The problem that this thesis encountered with FFT high pass filters was the excessive noise that was introduced in the images. The background noise was increased by a factor of nearly 1000 counts making the contrast much poorer than the original.

f) Contrast enhancement using the Mexican Hat Wavelet: Wavelets are a relatively recent mathematical tool used in the analysis of images, especially solar images. This thesis attempted this technique very successfully. Wavelets are wave representations which have both a frequency and time component that are retained in the signal they are convolved with. The wavelet used as primary convolution kernel is called the mother wavelet, here the mother wavelet is the Mexican hat wavelet provided by MaximDL. The wavelet was a level 5 wavelet with 5 levels of decomposition. The improvement in processed vs an unprocessed image is show in Figure 40

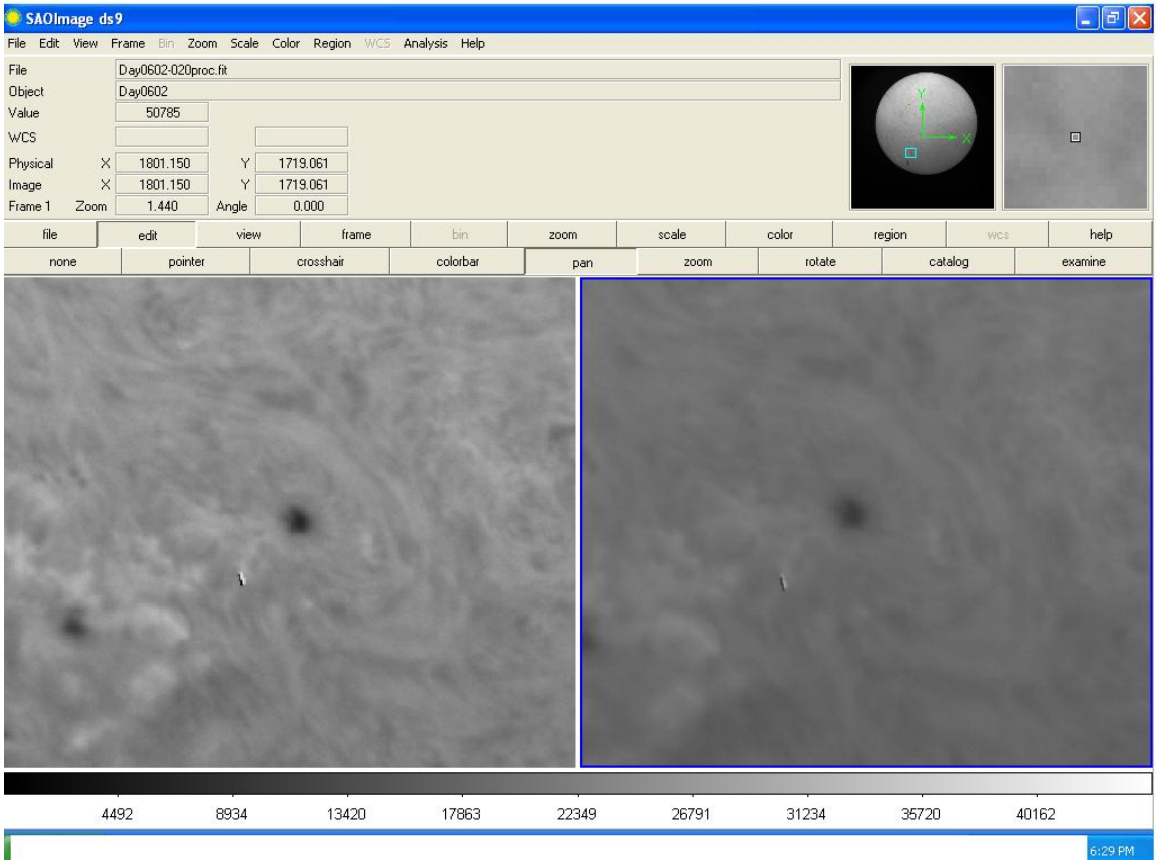

Figure 41: Wavelet processing on the left shows very clearly far more detail in the sunspot AR 11493, including a clear umbra and penumbra, along with the background chromosphere. This technique has produced some of the best results in terms of improving image quality. The change in radius is from 14.2 pixels in the original image to 17.4 pixels in the post-processed image, which is an increase of 2.3 arcseconds in the size of the spot.

This wavelet engine is readily available in the MaximDL wavelet toolkit. The wavelet is easy to apply and can provide upto 8 levels of decomposition. This thesis uses 5 levels of decomposition because anything higher than this does not make any significant change in the image to warrant the additional use of computing power. This image is then saved to a folder, for post-processing analysis. The analysis consisted of measuring the area of the spot before and after processing to estimate the change in size.

Procedure:

The data used in this processing consists of a total of 37 images from the observation on 06/02/2012. Before beginning the processing, the first task is to prepare the master flat. The master flat is prepared in MaximDL by selecting the calibration wizard option, selecting the files for flat fielding and then checking create master flat. This will create a master flat. Then the set of images which have to be used for processing are selected and flat divided using batch processing. The images are now ready to be processed.

The processing in this thesis is image to image, the overall image quality improves when the images are summed; however the idea here is to observe the change in seeing that varies from image to image. The image to be processed is opened in MaximDL and the wavelet option is selected from the filter menu. Once this is selected, MaximDL calculates the default decomposition matrix and displays the preview image as shown in Figure 41

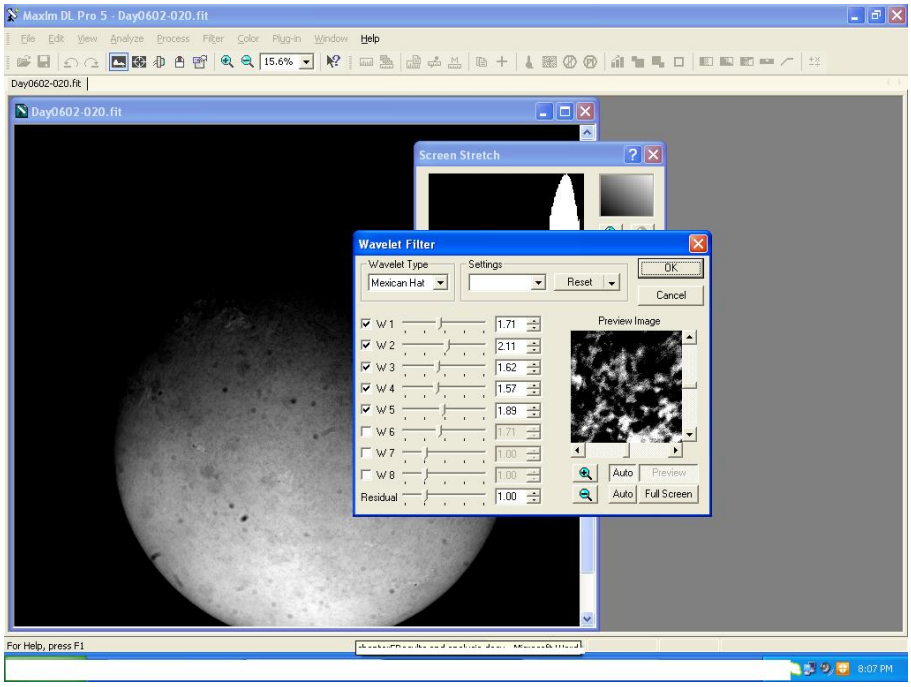

Figure 41: Wavelet processing. The wavelet procedure first calculates the default decomposition matrix shown on the left of the wavelet filter sub window. The preview image shows how these specific matrix elements can affect the image. The decomposition matrix can be varied by using the sliders.

Once the appropriate matrix is selected as shown in Figure 41, the wavelet is applied to the whole image. This requires some time as the whole procedure is mathematically intensive. It is important to note that better wavelet engines could be more efficient but the mathematical sophistication of the wavelet conceptually requires more processing power.

Once this is completed the image has been decomposed and re-composed from the wavelet coefficients and can be saved as the processed image.

To sum up the results of this exercise, Table 1 depicts all the algorithms used and gives the results of each algorithm succinctly.

Image processing technique used	Technique description	Result	Software used
Adaptive Histogram equalization	AHE is designed to enhance the local contrast of an image by altering the pixel values based on surrounding pixel values. The difference between the standard histogram equalization and AHE is that AHE improves the contrast by transforming each pixel with a transformation function derived from a neighborhood region	FAIL: This algorithm flattened the whole image uniformly making all the pixels the same value.	IDL
Robert's Edge enhancement algorithm	Like any edge enhancement algorithm it enhances the local discontinuities at the boundaries of different objects (edges) in the image. This algorithm has a different kind of kernel compared to other algorithms. This kernel focuses on the diagonal pixel differentials, which emphasizes corners more clearly but can blur together small horizontal or vertical features.	FAIL: The problem with this algorithm was that even though it brought out details, it wiped out most of the other features of the sun like gradation of color across the surface and opacity making the sun almost	IDL

		a transparent disc.	
Sobel's Edge enhancement algorithm	The Sobel's edge enhancement algorithm works the same way as the Robert's edge enhancement with the following kernels $\text{Y mask} = \begin{bmatrix} 1 & 2 & 1 \\ 0 & 0 & 0 \\ -1 & -2 & -1 \end{bmatrix}$ $\text{X mask} = \begin{bmatrix} -1 & 0 & 1 \\ -2 & 0 & 2 \\ -1 & 0 & 1 \end{bmatrix}$	FAIL: This transform enhanced the dust in the images over the actual features.	IDL
Unsharp mask	An unsharp mask is a two step process designed to improve image contrast. The procedure involves a) Creating a smoothed version of the original using a Gaussian blur b) compare the smoothed version to the original and if the difference is less than a specified threshold then the images are subtracted.	FAIL: The image processing in this case however produced an overall lowering of the intensity of the image. This was not acceptable as this was not representative of the original data that was recorded. The total max counts reduced from 25,000 to 9000.	IDL
High pass filter using kernels	The image processing in this case however produced an overall lowering of the intensity of the image. This was not acceptable as this was not representative of the original data that was recorded.	PASS: The radius of the spot pre processing is 23.4 pixels and the radius post processing is 26.86 pixels. This change corresponds to an increase of 2.5 arcseconds.	IDL
High pass filters	Fourier transforms applied to images result in the frequency responses of the individual pixels in the	FAIL: The background noise was increased by	MaximDL

	image. However, just transforming an image is not the objective, using the 100 FFT to retain just high frequency components of the image should lead to sharpening the image and enhancing the edges of the image. MaximDL applies the FFT and transforms the result back and mixes the result with the original image.	a factor of nearly 1000 counts making the contrast much poorer than the original.	
Contrast enhancement using Mexican Hat Wavelet	Wavelets are wave representations which have both a frequency and time component that are retained in the signal they are convolved with. The wavelet used as primary convolution kernel is called the mother wavelet, here the mother wavelet is the Mexican hat wavelet provided by MaximDL. The wavelet was a level 5 wavelet with 5 levels of decomposition.	PASS: The change in radius is from 14.2 pixels in the original image to 17.4 pixels in the post-processed image, which is an increase of 2.3 arcseconds in the size of the spot.	MaximDL

Table1: Description and results of all the image processing techniques used in this thesis.

Chapter 6 Conclusions and future work

This thesis has made the first effort at the UND Observatory to develop solar instrumentation and observing capabilities. The learning from this effort has been very interesting. Instrumentation does not come without problems and delays and this thesis has faced both quite amply. The key has been to persevere and look for solutions to problems, which have been posed by both the instrument and the data. Some problems have been solved and a great many have yet to be addressed. The problems that have to be addressed will form future project goals and hopefully will be solved in the near future.

A learning has been the variance in the seeing in the data. The variance in the seeing is seen to change from image to image. This does not form any kind of predictable pattern. The variance does not have any predictable periodicity; therefore it is much harder to generate atmospheric kernels that will eliminate this variance. This variance has been one of the preliminary problems observed in the data. The variance causes the same spot to appear entirely featureless in one image and suddenly show up a burst of features in the very next image.

The problem of the atmosphere at the UND Observatory has not been solved; however some image processing algorithms that could improve the contrast in the images

have been identified. The spot radius is but one of the ways to look at the improvement in quality of data, this is by no means the only indicator. Closer scrutiny of the data reveals that the processing techniques, especially wavelets, improves not just the size of the spot but it reveals hitherto invisible features like the penumbra and structure of the active region around the spot.

Identifying image processing algorithms and comparing the relative superiority has been another learning of this thesis. Out of the 7 algorithms implemented only 2 algorithms actually showed any kind of acceptable improvement. There were number of other tools such as the iImage of IDL which were attempted but did not lend the rigor necessary for the improvement of the image. The lack of enough wavelet engines to see the effect of different wavelets on the image was another issue faced in this thesis. IDL has a reasonably strong suite of wavelets, but they do not actually decompose and re-generate the original image but merely offer decomposition solutions. In future work one of the lines of work could be to find programs which can run the wavelet engines on 2D data. It is very clear from the preliminary processing that wavelets offer a high ability to improve the contrast in solar images.

Flat fielding is another area that can have a potential of future work. The flat fielding techniques have only been successful in removing few artifacts. Larger artifacts such as dirt on the image have not been removed subsequently they appear in the processed images as well. The overall image quality therefore remains poor. There is an urgent need to have flat fielding techniques that remove the artifacts and allow evaluation of overall image quality. The artifacts have also interfered with the processing on 06/02/2012 where one of the spots was very close to a piece of dirt on the image and

there was considerable fear of losing the spot in the dirt. A long term solution to this problem has yet to be found.

One of the future needs is that of a stable mount which can track better and offer more accurate pointing. The balance of the current Meade fork mount has also been very shaky. This is already in the works with quotes for a new mount being invited. The goal is to obtain a new Paramount MX for IO2. The arrival of a new mount with better balance and higher accuracy will make it much easier on the observer and will be one more step towards a more autonomous imaging set up.

Interacting with contractors like Daystar has been very difficult and at times extremely frustrating. A small miscommunication on the type of telescope resulted in the loss of nearly a year of observing time. This is an important future learning in that contractors have to be told more than once the needs of the observer, there needs to be repeated follow up and multiple cross checks to avoid this kind of miscommunication. In case of Daystar it was found that the fastest way to get a response for them was Daystar yahoo groups forum [http://tech.groups.yahoo.com/group/daystarfilters/].

In conclusion, the imaging from under the atmosphere is not only an issue because of day-to-day variations but is an issue because of image-to-image variations. This can be solved only with atmospheric kernels. The major imaging issue was the division of image artifacts like dirt from the image and the major observing issue faced here was the inaccurate tracking of the telescope.

Bibliography

Anderson, Lawrence S.; Athay, R. Grant. “Chromosphere and Coronal Heating”.The Astrophysical Journal vol 336. 1989. 1089-1091.

Andreas Lagg, Ryohko Ishikawa,Laura Merenda. "Internetwork Horizontal Magnetic Fields in the Quiet Sun Chromosphere: Results from a Joint Hinode/VTT Study." ASP Conference series, 2009.

Aschwanden, M. J. (2010). Image Processing techniques and Feature Recognition in Solar Physics. Solar Physics, 262, 235-275

Athay. R. G. “Hα and D3 profiles in chromospheric Spicules”. Annales D'Astrophysique.1958 pg 98-113.

Athay, R. G., & Thomas, R. N. (1961). “Physics of the solar chromospheres” New York: Interscience Publication.

Athay.R.G.. “The Origin of Spicules and Heating of the Lower Transition Region”. The Astrophysical Journal vol 287.1984. 412-417.

Athay.R.G.. “Are Spicules Related to Coronal Heating”. Solar Physics vol 197.2000.31-42.

Athay, R. G., & Thomas, R. N. (1961). Physics of the solar chromosphere. New York: Interscience Publication.

Bhatnagar, A., & Livingston, W. (2005). Fundamentals of Solar Astronomy. Denvers: World Scientific Publishing Co.

Beckers, Jacques M.; Tallant, Paul E..” Chromospheric Inhomogeneities in Sunspot Umbrae” Solar Physics,1969, Volume 7, Issue 3, pp.351-365

Bland, J., & Tully, R. B. (1989). The Hawaii imaging Fabry-Perot interferometer (HIFI). Astronomical Journal, 723-735.

Braun, D. C. & Birch, A. C.” Surface-Focused Seismic Holography of Sunspots: I. Observations” 2008, Solar Phys., 251, 267

Brosius, J. W., & Phillips, K. J. H. “Extreme-Ultraviolet and X-Ray Spectroscopy of a Solar Flare Loop Observed at High Time Resolution: A Case Study in Chromospheric Evaporation.” 2004, ApJ, 613, 580

Bruzek, A.: “Post-flare H-alpha plage formation.” 1972, Solar Phys. 26, 94.

Budnik,F.; Schroder,K.,-P.;Wilhelm,K.;Glassmier,K.-H.. “Observational evidence for coronal mass injection by “evaporation” of spicular plasma”.Astronomy and Astrophysics vol 334.1998.pg 77-80.

Daystar Filters. Quantum Hydrogen alpha filter. Daystar Filters, 2000.

Dere,K.,P.;Bartoe F.,-D.,J.;Brueckner,G.,E.. “High Resolution Telescope and Spectrograph observations of the Quiet Solar Chromosphere and the Transition Zone.”. The Astrophysical Journal vol 281.1983.pgs 870-883.

De Pontieu, B.. “Correlated Intensity oscillations in the Upper Chromospere and Upper Transition region above Active Region Plage”.ESASP vol 547. 2004.

De Pontieu, B.;Erdelyi. R.; De Moortel, I.. “HOW TO CHANNEL PHOTOSPHERIC OSCILLATIONS INTO THE CORONA”. The Astrophysical Journal vol 624.2005.61-64.

de Pontieu, B., McIntosh, S., Hansteen, V. H., Carlsson, M., Schrijver, C. J., Tarbell, T. D., . . . Nagata, S. (2007). A Tale of Two Spicules: The Impact of Spicules on the Magnetic Chromosphere. Publications of the Astronomical Society of Japan, 665-662

Denker, Carsten. “ Speckle Masking Imaging of Sunspots and Pores”. Solar Physics vol 180.1998.81-108.

Dumont, S. (1967). Formation des raies du Ca II et du Mg II dans la basse chromosphère. Annales d'Astrophysique, 421

Dunn,R. B.;1971;NBS Special Publication No. 353(Menzel Symposium); p.71

Edlen,B.,1942;Astrophysical Journal,105,323.

Ellerman, F., Astrophysical Journal, 47, 298 (1917)

Finger Lakes Instrumentation. (2006). Proline PL16803. New York: Finger Lakes Instrumentation.

Foukal P., and Lean J,. Astrophysics Journal, Vol 328 347-357, 1988.

Foukal, P. (1990). Solar astrophysics. New York: Wiley-Interscience.

Gadzhiev, T. G., & Nikolskii, G. M. (1982). Spicule Motions. Soviet Astronomy Letters, 341.

Georgoulis, Manolis K.; Rust, David M.;Bernasconi, Pietro N.; Schmieder, Brigitte.,The Astrophysical Journal, Volume 575, Issue 1, pp.506-528.

Hamilton, C. J. (2004, February 02). physics.montana.edu. Retrieved June 25, 2012, from http://solar.physics.montana.edu/ypop/Spotlight/SunInfo/Structure.html

Hindman, B. W. & Jain, R. 2008, ApJ, 677, 769

Howell, S. B. (2006). Handbook of CCD Astronomy. Cambridge: Cambridge University Press.

Ichimoto, K.; Kurokawa, H.. Solar Physics (ISSN 0038-0938), vol. 93, June 1984, p. 105-121.

Ishikawa, R., and S. Tsuneta. "Comparison of transient horizontal magnetic fields in a plage region and in the quiet Sun." Astronomy and astrophysics, 2008.

Jain, R., & Gordovskyy, M. (2008). On Absorption and Scattering of P Modes by Small-Scale Magnetic Elements. Solar physics, 361-368.

Jendersie, S.; Peter, H.;Astronomy and Astrophysics, Volume 460, Issue 3, December IV 2006. pp.901-908

Khomenko,E., and M. Collados The Astrophysical Journal, 689:1379Y1387, 2008 December 20

Khutsishvili, E. V. "Continuous Spectral Observations of Spicules.". Solar Physics vol 106.1985. pg 75-86.

Kitai, R.: 1983, Solar Phys. 87, 135.

Kneer, F.; Mattig, W.; v. Uexkuell, M. Astronomy and Astrophysics, vol. 102, no. 2, Oct. 1981, p. 147-155.

Knox,Keith T.,Thompson,Brian J.. "New Methods of Processing Speckle Pattern Star Images". The Astrophysical Journal vol 182.1973.133-136.

Kukhianidze, V., Zaqarashvili, T. V., & Khutsishvili, E. (2005). Kink Waves in Solar Spicules: Observation and Modelling. Proceedings of the 11th European Solar Physics Meeting, 64

Kulidzanishvili,V.,I.;Zhugzhuda, D.,YU.. "On the Problem of Spicular oscillations.".Solar Physics vol 88. 1983.35-41.

Labrosse, N., Heinzel, P., Vial, J.-C., Kucera, T., Parenti, S., Gunár, S., . . . Kilper, G. (2010).Physics of Solar Prominences: I—Spectral Diagnostics and Non-LTE Modelling. Springer, 243-332.

Labyerie.A.. "Attainment of Diffraction Limited Resolution in Large Telescopes by Fourier Analyzing Speckle Patterns in Star Images". Astronomy and Astrophysics vol 6. 1970. 85-87.

Lites, B. W.Astrophysical Journal, Part 1 (ISSN 0004-637X), vol. 301, Feb. 15, 1986, p. 992-1004.

Lockyer, J. N. (1868). Spectroscopic Observation of the Sun, No. II. Proceedings of the Royal Society of London, 131-132.

López Ariste, A., & Casini, R. (2005). Inference of the magnetic field in spicules from spectropolarimetry of He I D3. Astronomy and Astrophysics, 325-331.

Lyot, B., Annales d'Astrophysique, 7, 48 (1944).

Milligan, Ryan O.; Gallagher, Peter T.;The Astrophysical Journal, Volume 642, Issue 2, pp.L169-L171.

Moonglow Technologies, LLC. (2008). Interference Eliminator. Warrensburg: Moonglow Technologies.

Mullan, Dermott J."Physics of the Sun". CRC press. 2010 .ISBN 978-1-4200-8307-1

Nindos, Alexander; Zirin, Harold,. Solar Physics, v. 182, Issue 2, p. 381-392 (1998).\

Nikol'Skii, G. M., & Sazanov, A. A. (1967). The Motion and Nature of Hα Spicules in the Solar Chromosphere . Soviet Astronomy , 744.

Nikolsky,G.,M.. "The Observation of the chromospheric fine structure by the 53 cm Lyot coronagraph.". Solar Physics vol 12. 1970. pgs 379-390.

Nikolsky,G.,M.;Platova A.,G.. "Motions of Hα Spicules along the solar limb.". Solar Physics vol 18.1971.pgs 403-409.

Papushev, P. G., & Salakhutdinov, R. T. (1994). The dynamics of chromospheric spicules. Space Science Reviews , 47-51.

Pasachoff, J. M., Noyes, R. W., & Beckers, J. M. (1968). Spectral Observations of Spicules at Two Heights in the Solar Chromosphere. Solar physics, 131-158.

Preminger, D. G., Walton, S. R., & Chapman, G. A. (2001). SOLAR FEATURE IDENTIFICATION USING CONTRASTS AND CONTIGUITY. Solar Physics , 53-62.

Rust, D. M.: 1968, in K. O. Kiepenheuer (ed.), 'Structure and Development of Solar Active Regions', IAU Symp. 35, 77.

Ryan, Sean G., and Andrew J. Norton. Stellar Evolution and Nucleosynthesis. Cambridge university press, 2010.

Schott. (2008). Data Sheet. Schott.

Schrijver, C. J. & Title, A. M. 2003, ApJ, 597, L165

Severny, A. B., Astronomical Journal USSR, 33, 74 (1956).

Shine, Richard A.; Linsky, Jeffrey L. Solar Physics, Volume 25, Issue 2, pp.357-379,1972.

Shine, R. A., & Linsky, J. L. (1974). Physical properties of solar chromospheric plages. II - Chromospheric plage models. Solar Physics, 49-77.

Singh, J., Sakurai, T., Ichimoto, K., Suzuki, I., & Hagino, M. 2005, Sol. Phys., 226, 201

Smith, E Van P., 1969 ApJ.132, 202.

Sterling, A. C. (2009). Solar Spicules: A Review of Recent Models and Targets for Future Observations. Solar physics, 79-111.

Trujillo Bueno, J., Merenda, L., Centeno, R., Collados, M., & Landi Degl'Innocenti, E. (2005). The Hanle and Zeeman Effects in Solar Spicules: A Novel Diagnostic Window on Chromospheric Magnetism. ApJ, 191-194.

Turova, I. P.; Teplitskaia, R. B.; Kuklin, G. V..Solar Physics (ISSN 0038-0938), vol. 87, Aug. 1983, p. 7-22.

Turova, I. P.; Ozhogina, O. A.; Yurysheva, O. V.Solar Physics, Volume 227, Issue 1, 2005,pp.75-88

Vogt, S. S.; Penrod, G. D.. " Doppler Imaging of spotted stars - Application to the RS Canum Venaticorum star HR 1099" Astrophysical Journal vol. 95, Sept. 1983,p. 565-576.

Von der Lühe,O. “Speckle Imaging of Solar Small Scale Structure”.Astronomy and Astrophysical Journal vol 268. 1992.374-390.

Vorpahl, Joan; Pope, Thomas., Solar Physics, Volume 25, Issue 2, pp.347-356

Weart, S. R. (1970). The Horizontal Component of Spicule Motion. Solar physics, 310-314.

Zhang H., Ai, G., Wang, H., Zirin, H., and Patterson, A.: 1992, Solar Phys. 140, 307.

Zaqarashvili, T. V., Khutsishvili, E., Kukhianidze, V., & Ramishvili, G. (2007). Doppler-shift oscillations in solar spicules. Astronomy and Astrophysics, 627-632

Zirin, G. (1961). Magnetic Fields in Solar Prominences. Astronomicheskii Zhurnal, 861

Zirker ,J. B., “Spectral Observations of Solar Chromospheric Spicules”. Astrophysical Journals vol 136.1962. pg 250-263.

Zirker ,J. B., “Spectral Observations of Solar Chromospheric Spicules”. *Astrophysical Journals vol 136.*1962. pg 250-263.